國立交通大學

材料科學與工程研究所
博士論文

用於太陽電池之氮化矽次波長抗反射結構設計與樣品試製

Design and Fabrication of Sub-wavelength Structures on Silicon Nitride for Solar Cells

研 究 生：哥帝克

指導教授：張　翼 博士

中華民國九十八年十月

Design And Fabrication of Sub-wavelength Structures on Silicon Nitride for solar cells

研 究 生：哥帝克 Student: Kartika Chandra Sahoo

指導教授：張 翼 博士 Advisor: Dr. Edward Yi Chang

國立交通大學

材料科學與工程研究所

博士論文

A Dissertation

Submitted to Department of Materials Science and Engineering

College of Engineering

National Chiao Tung University

In Partial Fulfill of the Requirements

For the Degree of

Doctor of Philosophy

2009

Hsinchu, Taiwan, Republic of China

中華民國九十八年十月

Dedicated to

My Wonderful Parents

ACKNOWLEDGEMENT

This Ph.D. thesis was established in the Compound Semiconductor Devices Laboratory (Department of Materials Science & Engineering) at the National Chiao-Tung University (NCTU), and would not have been what it is today without the support and advice of others.

I first express my greatest gratitude and thankfulness to my advisor Prof. Edward Yi Chang, who supervised me during my entire Ph.D. study. Without his encouragement and inspiration, this work will never been done this far. His keen insights and intellectual comments have guided me throughout the ups and downs in my research. What I learned from him will benefit me for a life time as both an independent researcher and an active collaborator.

I would also like to thank Prof. Yiming Li of Department of Electrical Engineering, National Chiao-Tung University for his help in scientific and non-scientific advices. His valuable comments and training during the preparation of dissertation is appreciated.

I wish to thank former and current members in Compound Semiconductor Devices Laboratory of National Chiao-Tung University, Men-Ku Lin, S. P. Wang, C. C. Chen, Dr. Chun-Wei Chang, Dr. Yen Thomas, Chung-Yu Lu, Jui-Chien Huang, and

Dr. H. M. Lee. Discussions with them opened my viewpoints and inspired ideas. Many thanks to all the Ph.D. students and post-docs, past and present of the Compound Semiconductor Devices Laboratory, my office mate for more than five years, for the very nice working atmosphere and for the very good scientific discussions and contributions.

Furthermore, I want to thank National Science Council (NSC), Taiwan and Motech Industries Inc. (MOTECH), Taiwan for sponsoring our projects.

A special thank to my parents for their moral support and faith on me during all these years.

At last I wish to thank my lovely wife without whose support I couldn't have completed this thesis. Her constant encouragement and support during my ups and downs helps me to finish my work with productivity.

用於太陽電池之氮化矽次波長抗反射結構設計與樣品試製

研究生：哥帝克　　　　　　　　　　　　指導教授：張　翼　博士

國立交通大學材料科學與工程研究所

摘要

本論文首先以數值模擬計算太陽電池之氮化矽次波長抗反射結構。根據理論的分析，吾人進而發展樣品試製方法去製作氮化矽次波長結構。氮化矽是一種常用於半導體上的反射結構層材料，吾人藉此次波長結構當成第二抗反射層，使得完整樣品的結構爲雙層抗反射層。此種雙層抗反射結構成本低並具有不錯的太陽電池的光、電特性。

模擬上我們是使用嚴謹的波偶合法進行反射率計算，研究上吾人是對一理想化的金字塔型的氮化矽次波長抗反射結構進行反射率對照射波的計算。其中單層抗反射層、雙層抗反射層皆一一加以分析比較，進而找出較佳的幾何結構比，及其伴隨的有效反射率。藉由理論分析的結果，吾人運用自組裝鎳奈米粒子以及誘導式電漿離子偶合蝕刻提出一個簡單且可控制比例的製程步驟。藉此法在矽基板上以鎳薄膜厚度去控制鎳奈米粒子的大小與密度。由於次波長結構的表面形成與反應式離子蝕刻的條件密切相關，因此研究上也探討誘導式電漿離子偶合蝕刻製程條件對於氮化矽次波長抗反射結構成長的影響。吾人藉由實驗已找出蝕刻時間與結構幾何比例以及反射率的關係。

總之，本研究已經完成適用於太陽電池之氮化矽次波長抗反射結構的理論與實驗研究。未來可以研究不同次波長結構形狀的製程以及反射率之相關議題。

Design and Fabrication of Sub-wavelength Structures on Silicon Nitride for solar cells

Student: Kartika Chandra Sahoo Advisor: Dr. Edward Yi Chang

Department of Materials Science and Engineering
National Chiao Tung University

Abstract

In this dissertation, we numerically study the reflectance of sub-wavelength structures on silicon nitride for solar cell application. Based on the numerical study, we develop a fabrication method to form the sub-wavelength structures on silicon nitride surface for solar cells. Since silicon nitride is a well known antireflection coating used in semiconductor industry, we explore the texturization on silicon nitride antireflection coating and its optical properties. The main motivation behind this lies in the fact that the sub-wavelength structures will act as a second antireflection coating layer with an effective refractive index so that the total structure can perform as a double layer antireflection coating layer. Thus, we could cost down the deposition of second antireflection coating layer can be saved with better or comparable performance as that of a double layer antireflection coating solar cell.

In this study, we calculate the spectral reflectivity of pyramid-shaped silicon nitride sub-wavelength structures. A multilayer rigorous coupled-wave approach is advanced to investigate the reflection properties of silicon nitride sub-wavelength structure. We examine the simulation results for single layer antireflection and double layer antireflection coatings with sub-wavelength structure on silicon nitride surface, taking into account effective reflectivity over a range of wavelengths and solar efficiency. The results of our study show that a lowest effective reflectivity of 3.43% can be obtained for the examined silicon nitride sub-wavelength structure with the height of etched part of silicon nitride and the thickness of non-etched layer of 150 nm and 70 nm, respectively, which is less than the results of an optimized 80 nm silicon nitride single layer antireflection coating (~ 5.41%) and of an optimized double layer antireflection coating with 80 nm silicon nitride and 100 nm magnesium fluoride (~5.39%). 1% cell efficiency increase is observed for the optimized Si solar

cell with silicon nitride sub-wavelength structure, compared with the cell with single layer silicon nitride antireflection coatings; furthermore, compared with double layer antireflection coated solar cell, the increase is about 0.71%. The improvement on the cell efficiency is mainly due to lower reflectance of silicon nitride sub-wavelength structure over a wavelength region from 400 nm to 600 nm that leads to lower short circuit current.

Based upon our theoretical calculation of improved efficiency of silicon solar cell with silicon nitride sub-wavelength structures, we have developed a simple and scalable approach for fabricating sub-wavelength structures on silicon nitride by means of self-assembled nickel nano particle masks and inductively coupled plasma ion etching. The size and density of nickel nano particles are controlled by the initial thickness of nickel film that will be annealed to form the nano-particles on the silicon nitride film deposited on the silicon substrate. Inductively coupled plasma etching time is responsible for controlling the height of the fabricated silicon nitride sub-wavelength structure on silicon substrate.

Nevertheless, the surface profile of a sub-wavelength structure is strongly dependent on the conditions of the reactive ion etching process. So, we have also investigated the effect of inductively coupled plasma etching conditions on the profile of fabricated sub-wavelength structure on Silicon nitride antireflection coating layers. At last, we succeeded in fabrication of nanopillar structures and nanocone structures on silicon nitride surface by one step and two step inductively coupled plasma etching methods. The relationship of etching time with structure height and average reflectance spectra has been drawn.

In summary, design and fabrication of sub-wavelength structures on silicon nitride antireflective surface was investigated for the first time. The structure height and non-etched part of silicon nitride has been optimized for lowest effective reflectance by theoretical calculation using rigorous coupled wave analysis method. Also the shape effect has been studied theoretically. Based on theoretical results, the nanopillar and nanocone structures on silicon nitride surface have been fabricated successfully using self-assembled nickel nano clusters and inductively coupled plasma etching method. The achieved low reflectance is believed to be useful to improve the efficiency of solar cells. Also, the preliminary results for a silicon solar cell has been obtained using silicon nitride sub-wavelength structure, which shows a great promise in improvement of efficiency compared with a single layer antireflection coating.

Contents

Tables

Figures

Chapter 1

Introduction

Photovoltaic (PV), the direct conversion of sunlight into electric energy, is one component of an evolving energy mix. This technology provides several attractive features, such as pollution-free operation, relatively low maintenance costs, and modularity. In future energy scenarios solar cells (or PV cells) may well occupy an increasingly prominent role in global electricity generation in order to limit environmental pollution and to slow down the rate at which greenhouse gas concentration is rising. In recent studies, achieving higher efficiency in solar cells is the one of most important issues on the topic.

1.1 Introduction to solar cell

Semiconductor solar cells are fundamentally quite simple devices. Semiconductors have capacity to absorb light and to deliver a portion of energy of the absorbed photons to carriers of electrical current-electrons and holes. A semiconductor diode separates and collects the carriers and conducts the generated electrical current preferentially in a specified direction. Thus, a solar cell is simply a semiconductor diode that has been carefully designed and constructed to efficiently absorb and convert light energy from the sun into electrical energy.

A simple conventional solar cell structure is depicted in Figure 1.1 Sunlight is incident from the top on the front of the solar cell. A metallic grid forms one of the electrical contacts of the diode and allows the light to fall on the semiconductor between the grid lines and thus be absorbed and converted into electrical energy. The diode’s other electrical contact is formed by a metallic layer on the back of the solar cell.

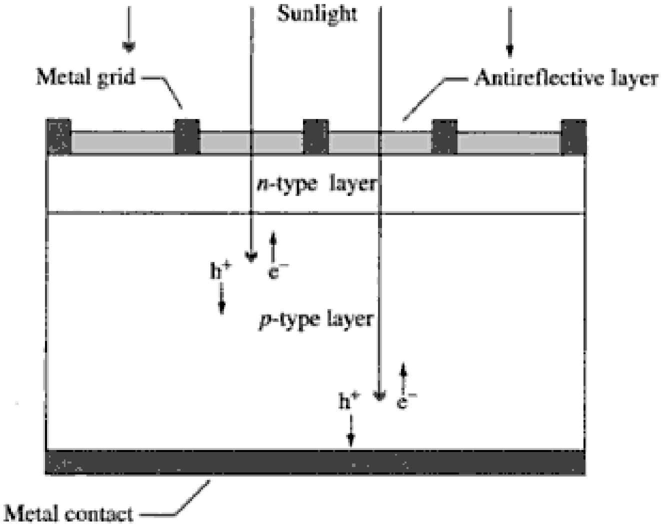

Figure 1.1 A schematic of simple conventional solar cell [50].

All electromagnetic radiation, including sunlight, is composed of particles called photons, which carry specific amounts of energy determined by the spectral properties of their source. Photons also exhibit a wavelike character with the wavelength, λ, being related to photon energy, E_{λ}, by

$$E_{\lambda} = \frac{hc}{\lambda} \tag{1}$$

Where h is planck's constant and c is the speed of light. Only photons with sufficient energy to create and electron-hole pair, that is, those with energy greater than the semiconductor band gap (E_G), will contribute to the energy conversion process. Thus, the spectral nature of sunlight is important consideration in the design of efficient solar cells.

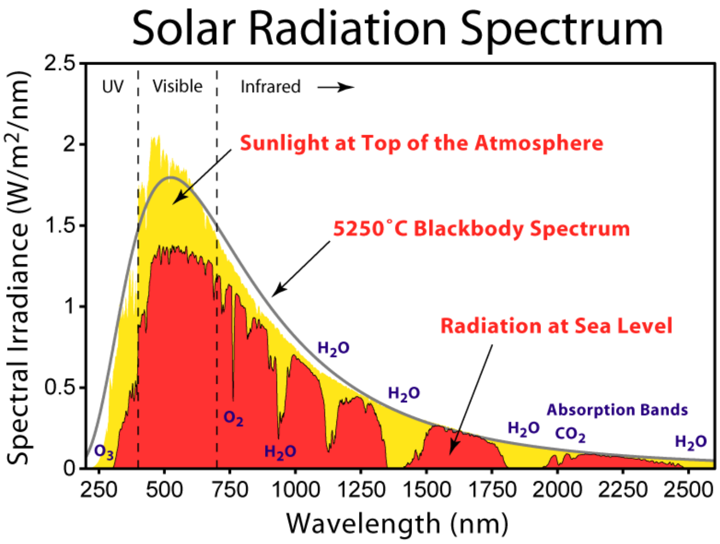

Figure 1.2 Solar Radiation Spectrum.

The sun has a surface temperature of 5762K and its radiation spectrum can be approximated by a black body radiator at that temperature. Emission of radiation from the sun is isotropic. However, the earth's great distance from the sun (~ 93 million miles) means that only those photons emitted directly in the direction of earth contribute to the solar spectrum as observed from the earth. Therefore, for practical purposes, the light falling on the earth can be thought of as parallel streams of photons. Just above the earth's atmosphere, the radiation intensity is about 135.3 mW/cm^2 [1] and the spectral distribution is referred to as an ***air mass zero*** (AM0) radiation spectrum. The Air Mass is a measure of how absorption in the atmosphere affects the spectral content and intensity of the solar radiation reaching the earth's surface. The Air Mass number is given by

$$Air\ Mass = \frac{1}{\cos\theta} \tag{2}$$

Where θ is the angle of incidence (θ = 0 when the sun is directly overhead). A widely used standard for comparing solar cell performance is the AM1.5 spectrum normalized to a total power density of 1kW/m^2.

1.2 Solar Cell figures of merit

1.2.1 Voltage and current

Two important quantities to characterize a solar cell are

Open circuit voltage (V_{oc}): The voltage between the terminals when no current is drawn (infinite load resistance)

Short circuit current (I_{sc}): The current when the terminals are connected to each other (zero load resistance)

The short circuit current increases with light intensity, as higher intensity mean more photons, which in turn mean more electrons. Since the short circuit current I_{sc} is roughly proportional to the area of the solar cell, the short circuit current density, $J_{sc} = I_{sc}/A$, is often used to compare solar cells.

When a load is connected to the solar cell, the current decreases and a voltage develops as charge builds up at the terminals. The resulting current can be viewed as a superposition of the short circuit current, caused by the absorption of photons, and a dark current, which is caused by the potential built up over the load and flows in the opposite direction. As a solar cell contains a PN-junction (LINK), just as a diode, it may be treated as a diode. For an ideal diode, the dark current density is given by

$$J_{dark}(V) = J_0\left(e^{qV/k_BT} - 1\right) \tag{3}$$

Here J_0 is a constant, q is the electron charge and V is the voltage between the terminals. The resulting current can be approximated as a superposition of the short circuit current and the dark current:

$$J = J_{SC} - J_0\left(e^{qV/k_BT} - 1\right) \tag{4}$$

To find an expression for the open circuit voltage, V_{oc}, we use (4) setting J = 0. This means that the two currents cancel out so that no current flows, which exactly is the case in an open circuit. The resulting expression is

$$V_{OC} = \frac{k_B T}{q} \ln\left(\frac{J_{SC}}{J_0} + 1 \right) \tag{5}$$

1.2.2 Efficiency

In general, the power delivered from a power source is P = IV, i.e. the product of voltage and current. If we instead use the current density J, we get the power density:

$$P_d = JV \tag{6}$$

The maximum power density occurs somewhere between V = 0 (short circuit) and V = V_{oc} (open circuit) at a voltage V_m. The corresponding current density is called J_m, and thus the maximum power density is $P_{d,m} = J_m V_m$.

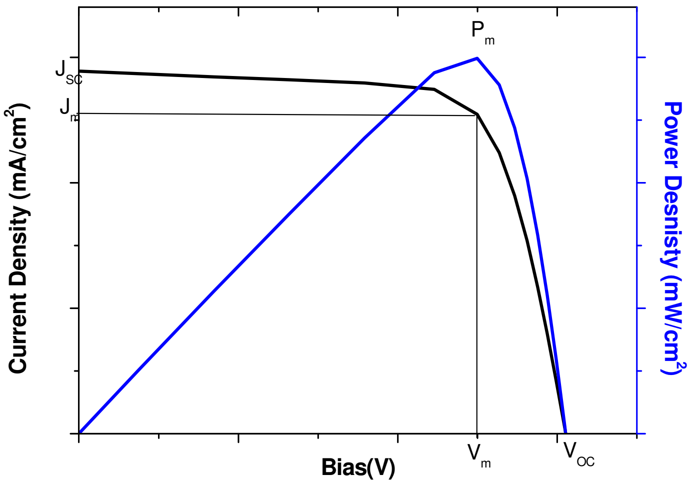

Figure 1.3: J~V characteristics and Maximum power

The efficiency of a solar cell is defined as the power (density) output divided by the power (density) output. If the incoming light has a power density Ps, the efficiency will be

$$\eta = \frac{J_m V_m}{P_s} \tag{7}$$

The fill factor, FF, is another quantity which is used to characterize a solar cell. It is defined as

$$FF = \frac{J_m V_m}{J_{SC} V_{OC}} \tag{8}$$

and gives a measure of how much of the open circuit voltage and short circuit current is "utilized" at maximum power. Using FF we can express the efficiency as

$$\eta = \frac{J_{SC} V_{OC} FF}{P_s} \tag{9}$$

The four quantities J_{sc}, V_{oc}, FF and η are frequently used to characterize the performance of a solar cell. They are often measured under standard lighting conditions, which implies Air Mass 1.5 spectrum, light flux of 1000W/m^2 and temperature of 25°C.

1.2.3 Natural Limits of Efficiency

In addition to optimizing the production processes, work is also being done to increase the level of efficiency, in order to lower the costs of solar cells. However, different loss mechanisms are setting limits on these plans. Basically, the different semiconductor materials or combinations are suited only for specific spectral ranges. Therefore a specific portion of the radiant energy cannot be used, because the light quanta (photons) do not have enough energy to "activate" the charge carriers. On the other hand, a certain amount of surplus photon energy is transformed into heat rather than into electrical energy. In addition to that, there are optical losses, such as the shadowing of the cell surface through contact with the glass surface or reflection of incoming rays on the cell surface. Other loss mechanisms are electrical resistance losses in the semiconductor and the connecting cable. The disrupting influence of material contamination, surface effects and crystal defects, however, are also significant. Single loss mechanisms (photons with too little energy are not absorbed, surplus photon energy is transformed into heat) cannot be further improved because of inherent physical limits imposed by the materials themselves. This leads to a theoretical maximum level of efficiency, i.e. approximately 28% for crystalline silicon.

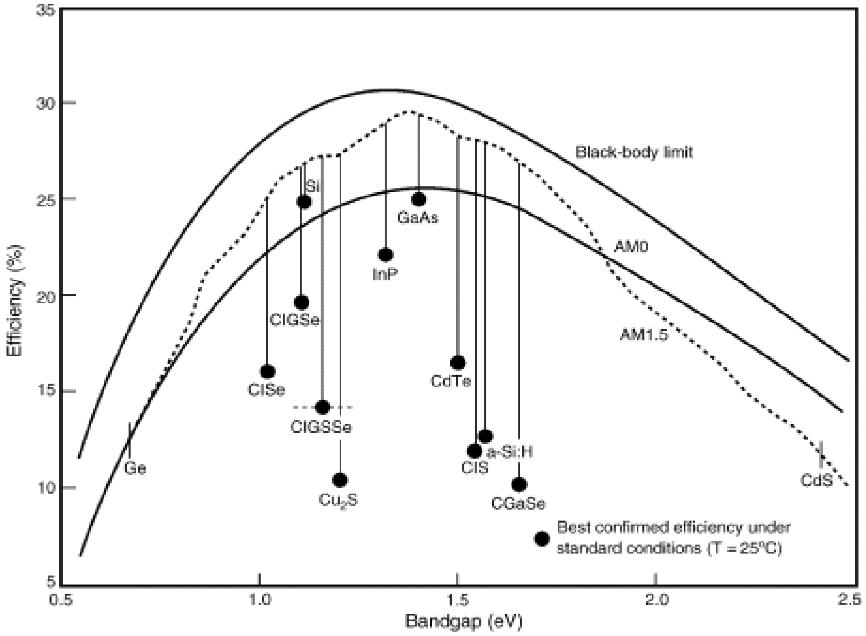

Figure 1.4: Theoretical maximum levels of efficiency of various solar cells at standard conditions [51].

To maximise current density J_{PV} it is necessary

- maximise generation rate G
- minimise recombination rate

Generation rate is given by

$$G(\lambda;x)=\left(\frac{d\Delta n}{dt}\right)_{gen}=\alpha(\lambda)\beta(\lambda)\Phi(\lambda;x)$$
$$=\alpha(\lambda)\beta(\lambda)\Phi_0(\lambda)\exp\left(-\alpha(\lambda)x\right) \quad (10)$$

Where, $\phi_0 = \phi_{in}(1-R)$ (11)

Where, α is absorption co-efficient, ϕ is no of photons incident.

So from equation 10 and equation 11, it is seen that generation rate depends on the no of photons, absorption co-efficient, thickness of material, and reflection. So, to maximize generation rate it is necessary to minimize surface reflection, especially in the visible region of solar spectrum as shown in Figure 1.5.

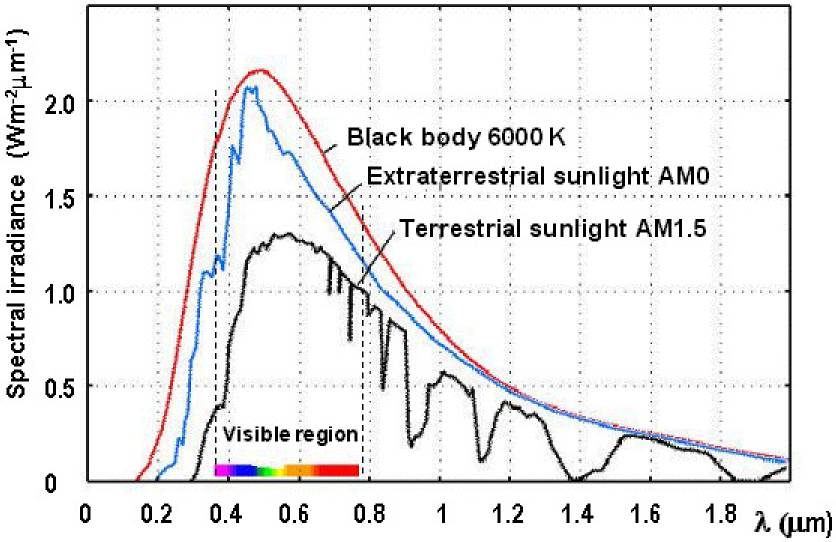

Figure 1.5: Solar Spectrum [50].

Since, Silicon and III-V materials are generally used for high efficiency solar cell and these semiconductor materials have high refractive index [2]. As per Fresnel equation, there is over 30% of solar spectrum reflected by surface and energy is wasted. So, to improve the cell efficiency, we need to reduce reflection and increase the absorption.

The methods to reduce reflection are:

1. **Anti-reflection coatings**
2. **Sub-wavelength Structures**

1.3 Antireflection Coatings

1.3.1 Single Layer Antireflection Coatings

Anti reflective coatings (ARCs) are types of optical coating applied to lenses and other devices to reduce reflection from optical surfaces. It's a popular strategy to place ARCs on light detecting devices to improve device quantum efficiency. Such coatings rely on destructive interference of reflected waves to reduce overall reflection coefficient of light on the detecting device.

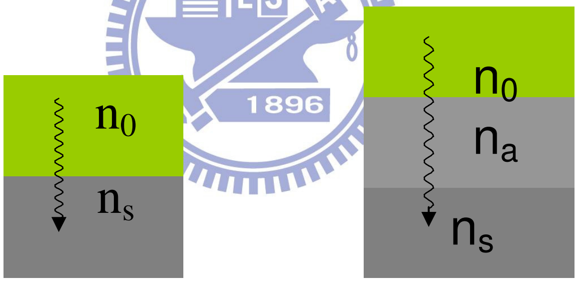

Fig. 1.6: Schematic of different material structure (a) two layers without ARC (b) Three layers with ARC

A single layer coating on a substrate is shown in Fig. 1.6 (a). The refractive indices of the surrounding medium and the substrate are n_0 and ns, respectively. Now suppose light falls from top and passes through the two medium. Then from the Fresnel's principle the fraction of photons reflected at the interface between two medium with different refractive indices is given by

$$R = \left[\frac{n_s - n_0}{n_s + n_0} \right]^2 \tag{11}$$

Silicon’s high index of refraction varies from n = 3.5 at 1.1 μm (infrared) to n = 5.6 at 0.4 μm (violet), and produces a large reflection coefficient across the solar spectrum: 34 % at 1.1μm increasing to 54 % at 0.4 μm. Any mechanism that increases the coupling of light in to the silicon surface improves the short-circuit current of silicon solar cell. There are two approaches: texturing of the surface to produce multiple reflections back into the silicon and creation of matching section (ARCs) to lower the reflection coefficient.

Now let’s use another layer3 as ARC with refractive index n_a in between layer1 and layer2 as shown in figure 1.6 (b). Now the equation (1.6) will become

$$R = \left[\frac{\left(n_0 n_s - n_a^{\,2}\right)}{\left(n_0 n_s + n_a^{\,2}\right)} \right]^2 \tag{12}$$

The necessary and sufficient conditions for a single-layer coating to produce zero reflectance are:

$$n_a = (n_0 n_s)^{1/2},\ n_a < n_s \tag{13}$$

and

$$d = \frac{\lambda}{4 n_a} \tag{14}$$

Where d is the antireflection layer thickness and λ is the wavelength of the incident light.

From equation (14) the optical thickness $n_a d$ is then one quarter wavelength of the incident light. This antireflection coating is known as a quarter-wave coating. The reflectance of quarter wave coating is equal to zero at the wavelength corresponding to optical thickness of quarter wavelength, if equation (13) is satisfied. If equation (13) is not satisfied, then the reflectance will indicate a minimum at the same wavelength.

The position of the reflectance minimum of a surface coated with a quarter-wave coating depends on the optical thickness of the coating and shifts towards longer wavelengths as the optical thickness increases. The effectiveness of a single-layer antireflection coating is limited by the available materials with suitable index.

Moreover, zero or minimum reflectance can be obtained at only one wavelength and the reflectance increases rapidly on both side of the zero or minimum position. Several transparent and high refractive-index material films have already been applied to ARC techniques, e.g. SiO (n=1.8–1.9), SiO_2 (n=1.44), Si_3N_4 (n=1.9), TiO_2 (n=2.3), Al_2O_3 (n=1.86), Ta_2O_5 (n=2.26), and SiO_2–TiO_2 (n=1.8–1.96) [3-8].

For application of high efficiency solar cell, we always demand a broadband and Omni directional antireflection layer [9]. These difficulties can be largely overcome by using coatings with two or more layers.

1.3.2 Multi-layer Antireflection Coatings

Multiple layers are more effective over the entire visible spectrum. For the double-layer ARC design, the low–high index on the Si substrate (i.e., the outer layer has the low refractive index and inner layer has high refractive index) is used. Figure 1.7 (a) and (b) show the typical double and triple layer antireflection coatings structure [Multilayer]. The principle of this type of ARC has been illustrated using the vector methods previously [10-12].

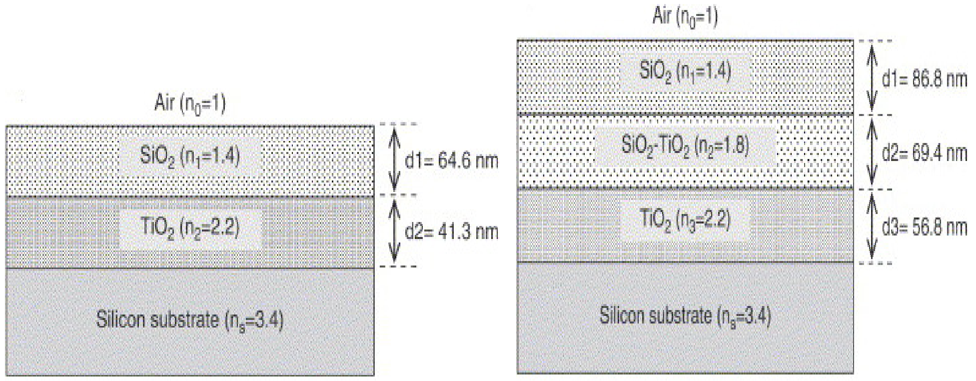

(a) (b)

Figure 1.7 Diagram of antireflection coatings with (a) SiO_2/TiO_2 double layers and (b) $SiO_2/SiO_2–TiO_2/TiO_2$ triple layers.

Optical coatings are generally performed by vacuum processes such as thermal evaporation, reactive sputtering, and plasma-enhanced chemical vapor deposition (PECVD). All these methods are capable of producing films with uniform thickness and good optical properties. However, the conventional vacuum deposition processes are expensive and unsuitable for continuous mass production techniques in low-cost solar cells. So, these multilayer antireflection coatings (ARCs) are expensive to fabricate owing to the stringent requirement of high vacuum, material selection, and layer thickness control. Also additional problem of thermal mismatch between different layers and difficulties with the availability of materials with suitable optical properties arises in case of multilayer ARCs.

1.4 Sub-wavelength Structures

An alternative to multilayer ARCs is the sub-wavelength structures (SWS) surface with dimensions smaller than the wavelength of light. SWSs are zero order grating structures with the period of grating is much smaller than incident wavelength so that there will be only one reflected wave and one transmitted wave as shown in

Figure 1.8. Other high-order diffracted waves are forced to be evanescent. An electromagnetic wave propagates through a sub-wavelength or zero-order grating in approximately the same manner that it propagates through a homogeneous non-corrugated medium [13].

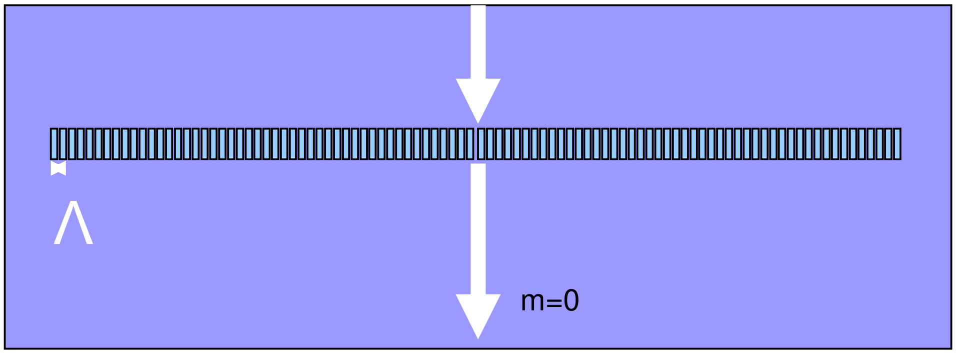

Figure 1.8 Schematic of a Sub-wavelength grating structure

In publications concerning broadband or solar antireflection surfaces [14-17], the principle to achieve the necessary low refractive indices is always the same: substrate material is mixed with air on a sub-wavelength scale. To date, a wide variety of techniques were examined for texturing microcrystalline-Si cells [18-21]. One of promising options is surface texturing by dry etching technique. Fabricating uniform textures with a submicron scale on mc-Si wafers by reactive ion etching (RIE) for Si solar cells [22-23] has been studied. But, this forms the dislocations and defects in the semiconductor layer. These defects and dislocations are responsible for increasing the minority carrier recombination in solar cell. Thus, the short circuit current for the solar cell is decreased, which in turn decreases the efficiency of solar cell.

1.5 Motivation

Therefore, key issues need to be solved:

(1) It is necessary to find a way to form the sub-wavelength structure which can reduce reflectance and reduce the damage created by RIE method.

(2) It is necessary to find the way to replace the deposition of second ARC layer so that we can low down the cost of deposition of another layer and thermal mismatch.

(3) It is necessary to develop a low cost and easy fabrication method to form the sub-wavelength structure on antireflection coating.

Therefore, we studied the possibility of sub-wavelength structure on ARC surface instead of semiconductor surface, which may benefit the Si solar cell technologies. We chose to study the silicon nitride (Si_3N_4) sub-wavelength structure for this study due to the following reasons:

(1) Si_3N_4 is a well-known ARC used in semiconductor industry.

(2) No previous studies about solar cell with Si_3N_4 SWS.

(3) Sub-wavelength structures will act as a second ARC layer with an effective refractive index so that the total structure can perform as a double layer antireflection layer (DLAR) layer.

(4) Si_3N_4 SWS will avoid or reduce the problem of defects created in Si and will improve the efficiency of Solar Cell.

In this work, we calculate the spectral reflectivity of pyramid-shaped Si_3N_4 sub-wavelength structures (SWS). A multilayer rigorous coupled-wave approach is advanced to investigate the reflection properties of Si_3N_4 SWS. We examine the simulation results for single layer antireflection (SLAR) and DLAR coatings with SWS on Si_3N_4 surface, taking into account effective reflectivity over a range of wavelengths and solar efficiency. Also we compare the pyramid-shaped structures with cone, parabola, and cylinder-shaped SWS to see the effect of shapes on reflectance property of SWS.

Based upon our theoretical observation efficiency of silicon solar cell with silicon nitride SWS, we develop a simple and scalable approach for fabricating sub-wavelength structures (SWS) on silicon nitride by means of self-assembled nickel nano particle masks and inductively coupled plasma (ICP) ion etching. The size and density of nickel nano particles is optimized by considering different parameters.

Nevertheless, the surface profile of a sub-wavelength structure is strongly dependent on the conditions of the RIE process. So, we investigate the effect of ICP etching conditions on the profile of fabricated sub-wavelength structure on Silicon nitride antireflection coating layers.

1.6 Thesis content

The introduction to solar cell, the need of sub-wavelength structure and the motivation for this work has been described in chapter 1.

In chapter 2, the theory and design of sub-wavelength structure developed in our work has been described. Modeling of sub-wavelength structures via effective medium theories is examined. Also, we will describe about PC1D calculation method of solar cell characteristics and the results in this chapter.

A detail description of our developed fabrication method and results for silicon nitride sub-wavelength structure is given in chapter 3. Furthermore, the description of the instruments used in process and measurement are given in this chapter.

In chapter 4, the fabrication methods of silicon nitride nanocone structures are described with detail fabrication mechanism. Also the results are analyzed in the chapter.

In chapter 5, we will describe the results of fabricated solar cell using silicon nitride sub-wavelength structures in briefly.

Then, in the final chapter, we will summarize and conclude our studies and findings. Some suggestions for future studies will also be given for the improvement of the silicon nitride sub-wavelength structures.

Chapter 2

Design and Simulation of Silicon Nitride SWS

It is necessary to study the reflectance properties of the silicon nitride sub-wavelength structures on silicon substrate with different shapes and optimize the structure height for the better average reflectance before studying the sub-wavelength structures experimentally. So in this chapter, the theory of the developed model for the study of sub-wavelength structures has been described in details with the results and their discussions. Also the procedure of electrical characteristics calculation of a silicon solar cell using the sub-wavelength structure and the results has been reported in this chapter.

2. 1 Sub-wavelength structure design

2.1.1 Theory and Simulation Procedure

For the simplicity, a single pyramidal structure, shown in Fig. 2.1(a), is explored for the reflectance property with respect to the wavelength. The region with brown color of SWS is Si_3N_4, the region with sky color stands for Si substrate, and the environment of the triangular part is air. The etched Si_3N_4 (i.e., the height of triangular part) is h and the thickness of the non-etched Si_3N_4 is s, both of these two parameters are designing parameters for the reflectance optimization.

The studied SWS is a diffractive structure and its reflectance property could be calculated by a rigorous coupled-wave analysis (RCWA) technique. RCWA is an exact solution of Maxwell's equations for the electromagnetic diffraction by grating structures. A multilayer RCWA method is used in this study, where the effective medium theory (EMT) [24-26] is adopted to calculate the effective refractive index for each partitioned uniform homogeneous layer, as shown in Fig. 2.1(b).

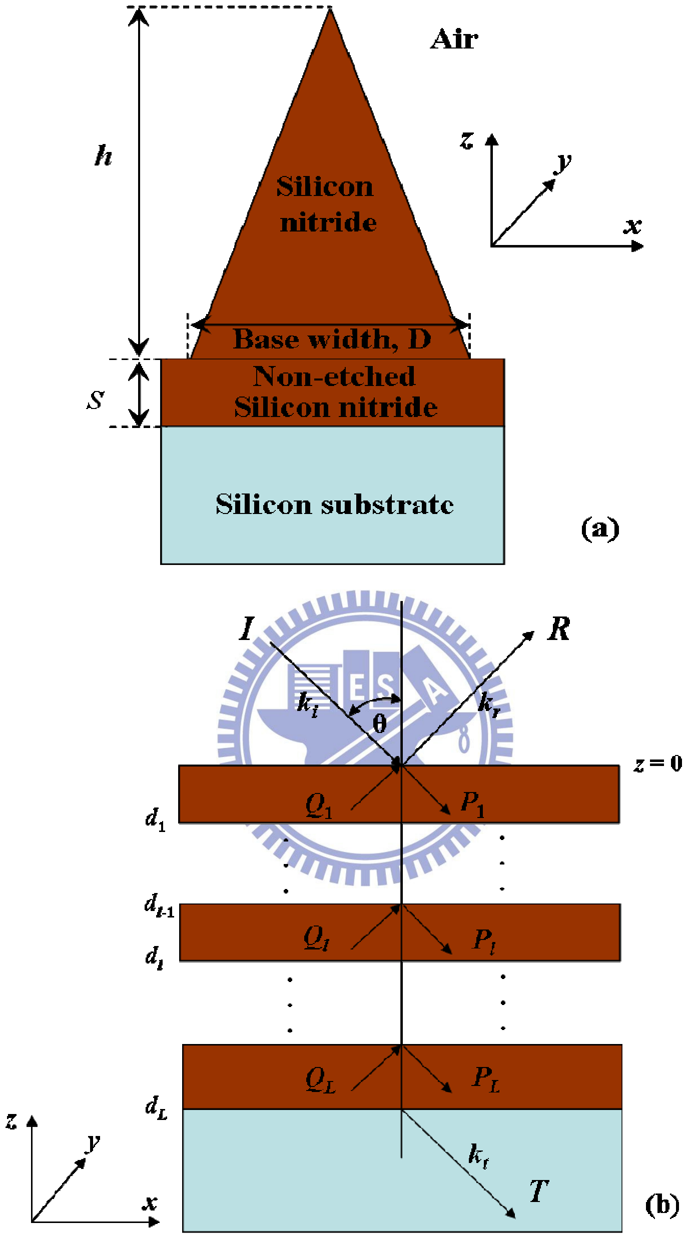

Figure 2.1: (a) Geometry of sub-wavelength structure studied in this work, where *h* is the height and s is the non-etched part of SWS. (b) A stack of uniform homogeneous layers resulting from the partitioned geometry of (a) for the reflection calculation using the multilayer RCWA method and EMT.

Simplifications of Maxwell’s equations are based on the following assumptions:

1. **Incident field is an arbitrary linearly polarized monochromatic plane wave**
2. **Electromagnetic fields are time-harmonic**
3. **Media are linear, homogeneous and isotropic**
4. **Gratings are infinitely periodic and are approximated with a layered structure**

Reducing the computational domain to one unit-cell, without loss of generality (WLOG), we first divide the pyramidal structure into several horizontal layers with equal thickness. As shown in Fig. 2.1(b), for each discreted position z_l along the z direction, EMT implies that the effective refractive index $n(z_l)$ of each layer is approximated by

$$n(z_l)=\sqrt{\frac{\left[1-f(z_l)+n_{SiN}^2\right]\left[f(z_l)+\left(1-f(z_l)\right)n_{SiN}^2\right]+n_{SiN}^2}{2\left[f(z_l)+\left(1-f(z_l)\right)n_{SiN}^2\right]}}, \tag{15}$$

where, $f(z_l)$ is the fraction of Si_3N_4 contained in each layer and is given by,

$$f(z_l)=\frac{4r_l^2}{\sqrt{3}D^2} \tag{16}$$

r_l is the base width for each layer and is given by

$$r_l=r\left(1-\frac{z_l}{h}\right) \tag{17}$$

and D is the base width of the structure, $n_{SiN}=n+ik$ is the complex refractive index of Si_3N_4, $i=\sqrt{-1}$, n and k are optical constants, and $n_{air}=1$ is the refractive index of air. Note that only the real part of refractive index of Si_3N_4 is considered in our simulation because it is weakly absorbing material [27]. With the calculated effective refractive index $n(z_l)$ for each layer, we can solve the reflectance property of the entire structure including a layer for the non-etched Si_3N_4 with respect to the different wavelength.

From the partitioned structure, shown in Fig. 2.1(b), we now consider the reflection and the transmission of a transverse electric (TE) polarized plane wave of free-space wavelength λ, incident at angle θ, on L uniform layers of effective refractive indices $n_1 = n(z_1)$, …, n_l, …, $n_L = n(z_L)$ and thickness d_1, …, d_l, …, d_L. For each layer, the normalized electric field (in the x-y plane) for the input and the output regions is given by, for the air region, i.e., $z \le 0$

$$E_0 = (e^{-ik_{air,z}z} + R \times e^{-ik_{air,z}z})e^{-ik_x x}, \tag{18}$$

for the region of SWS, i.e., $D_{l-1} \le z \le D_l$,

$$E_l = (p_l \times e^{-ik_0\gamma_l(z-D_{l-1})} + Q_l \times e^{ik_0\gamma_l(z-D_l)})e^{-ik_x x}, \tag{19}$$

and for the Si substrate, i.e., $z \ge D_L$,

$$E_t = T \times e^{-i(k_x x + k_{Si,z}(z-D_L))}, \tag{20}$$

Where,

$$k_x = k_0 n_{air}\sin\theta, \tag{21}$$

$$k_{air,z} = k_0 n_{air}\cos\theta, \tag{22}$$

$$k_{Si,z} = k_0\sqrt{n_{Si}^2 - n_{air}^2\sin^2\theta}, \tag{23}$$

$$\gamma_l = i\sqrt{n_l^2 - n_{air}^2\sin^2\theta}, \tag{24}$$

$$D_l = \sum_{p=1}^{l} d_p, \tag{25}$$

l = 1, …, L, I, R and T are the incident, reflected and the transmitted amplitudes of the electric fields, P and Q are the field amplitudes in the uniform Si_3N_4 slab, $k_0 = 2\pi/\lambda$

is the wave-vector magnitude, and n_{air} and n_{Si} are the refractive indices of the air and the silicon regions. Note that now the layer of non-etched Si_3N_4 has been added into our simulation structure, where its effective refractive index $n_{SiN} = 2.05$ is the same with the original one and $f(z_L) = 1$. The reflected and transmitted amplitudes of the explored SWS are calculated by matching the tangential electric- and magnetic-field components at the boundaries among layers [28]. First, for the boundary between the input air region and the first layer of Si_3N_4 (i.e., $z = 0$), we have

$$\begin{cases} 1 + R = P_1 + Q_1 \times e^{-k_0\gamma_1 d_1} \\ i\dfrac{k_{air,z}}{k_0}(1 - R) = \gamma_1 (P_1 - Q_1 \times e^{-k_0\gamma_1 d_1}) \end{cases} . \tag{26}$$

For the boundary between the $(l - 1)^{st}$ and the l^{th} layers (i.e., $z = D_{l-1}$)

$$\begin{cases} P_{l-1} \times e^{-k_0\gamma_{l-1} d_{l-1}} + Q_{l-1} = P_l + Q_l \times e^{-k_0\gamma_l d_l} \\ \gamma_{l-1}(P_{l-1} \times e^{-k_0\gamma_{l-1} d_{l-1}} - Q_{l-1}) = \gamma_l (P_l - Q_l \times e^{-k_0\gamma_l d_l}) \end{cases} ; \tag{27}$$

for the boundary between the last layer and the output Si region (i.e., $z = D_L$), the matched equations are

$$\begin{cases} P_L \times e^{-k_0\gamma_L d_L} + Q_L = T \\ \gamma_L (P_L \times e^{-k_0\gamma_L d_L} - Q_L) = i(\dfrac{k_{Si,z}}{k_0})T \end{cases} . \tag{28}$$

The equations (26)-(28) could be solved by using a transmittance matrix method [29]. Using Eq. (28), the field amplitudes P_L and Q_L in terms of the transmitted coefficient T are determined firstly. They are then substituted into Eq. (27) for the field amplitudes P_{L-1} and Q_{L-1}. Consequently, the system of equations to be solved for the reflection properties is given by

$$\begin{bmatrix}1\\ i\frac{k_{air,z}}{k_0}\end{bmatrix}+\begin{bmatrix}1\\ -i\frac{k_{air,z}}{k_0}\end{bmatrix}R=\prod_{l=1}^{L}\begin{bmatrix}1 & e^{-k_0\gamma_l d_l}\\ \gamma_l & -\gamma_l e^{-k_0\gamma_l d_l}\end{bmatrix}\times\begin{bmatrix}e^{-k_0\gamma_l d_l} & 1\\ \gamma_l e^{-k_0\gamma_l d_l} & -\gamma_l\end{bmatrix}^{-1}\times\begin{bmatrix}1\\ i\frac{k_{Si,z}}{k_0}\end{bmatrix}T\ ,(29)$$

for partitioned layers of SWS. Similarly, a set of governing equations could be derived for the transverse magnetic (TM) polarization. Here the incident angle θ of sun light is assumed to be normal to the plane (i.e., $\theta = 0^o$), and only the TE polarization is considered here for the calculation of the reflection properties [30].

For a given number of layers for the SWS including the layer of non-etched Si_3N_4, say L in total; a calculation procedure for computing the reflectance properties of the studied SWS described above is summarized: (i) calculate the effective refractive index for each z_l via Eq. (1); (ii) compute the coefficients using Eqs. (21)-(25) for a specified wavelength λ; (iii) and solve Eq. (29) to get the unknowns R and T.

2.1.2 Results and Discussions

First of all, we compare the reflectance with respect to the wavelength of sunlight for the SWS with Si and Si_3N_4. As shown in Figure 2.2(a), by assuming a constant refractive index for Si $n_{Si} = 3.875$ and for Si_3N_4 $n_{SiN} = 2.05$, the reflectance versus the wavelength for Si SWS with h = 88 nm and Si_3N_4 SWS with h = 88 nm and vanished non-etched part of SWS (i.e., s = 0 nm) is simulated and compared.

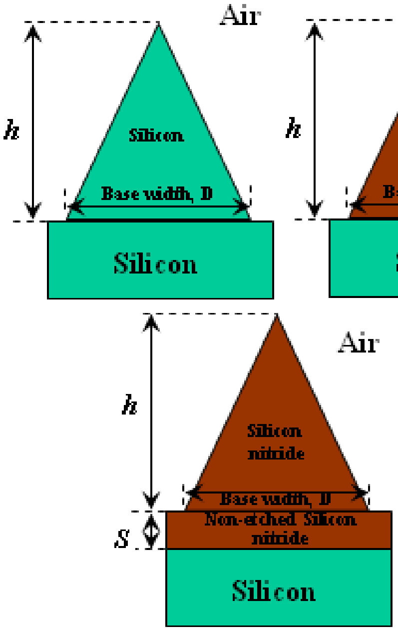

(a)

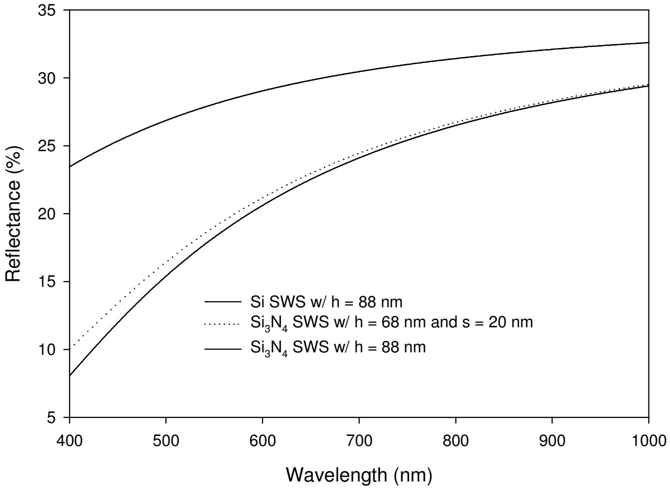

(b)

Figure 2.2: (a) The schematic of Si and Si_3N_4 SWS for the study. (b) The reflectance versus the wavelength for Si SWS with *h* = 88 nm and Si_3N_4 SWS

with *h* = 88 nm and vanished non-etched part of SWS (i.e., s = 0 nm). Comparison for the Si_3N_4 SWS with the case of non-zero *s*, say *s* = 20 nm is also provided. It is found that it is possible to reduce the reflectance of Si_3N_4 SWS by proper selection of *h* and *s*.

As seen from Figure 2.2(b), it is found that the non-optimized Si_3N_4 SWS possesses a little bit higher reflectance which may not be a plus for ARC. However, we can design a Si_3N_4 SWS with the case of non-zero s, say h = 68 nm and s = 20 nm, which shows that the reflectance is close to the result of Si SWS or even better. This observation motivates us to explore the morphology-dependent reflectance of Si_3N_4 SWS with a set of optimized h and s. Note that Si refractive index n_{Si} may depend upon the wavelength of incident sunlight [31]; our calculation for the Si_3N_4 SWS with h = 68 nm and s = 20 nm confirms the reflectance difference between the model with constant and wavelength-dependent n_{Si}, as shown in Figure 2.3. In this calculation, an empirically fitted formula for the wavelength-dependent n_{Si} is implemented in our simulation program [32]

$$n_{Si} = \sqrt{\varepsilon + \frac{A}{\lambda^2} + \frac{B\lambda_1^2}{\left(\lambda^2 - \lambda_1^2\right)}}, \qquad (30)$$

where, λ_1 = 1.1071 μm, ε = 11.6858, A = 0.939816 μm^2 and B = 8.10461 × 10^{-3}.

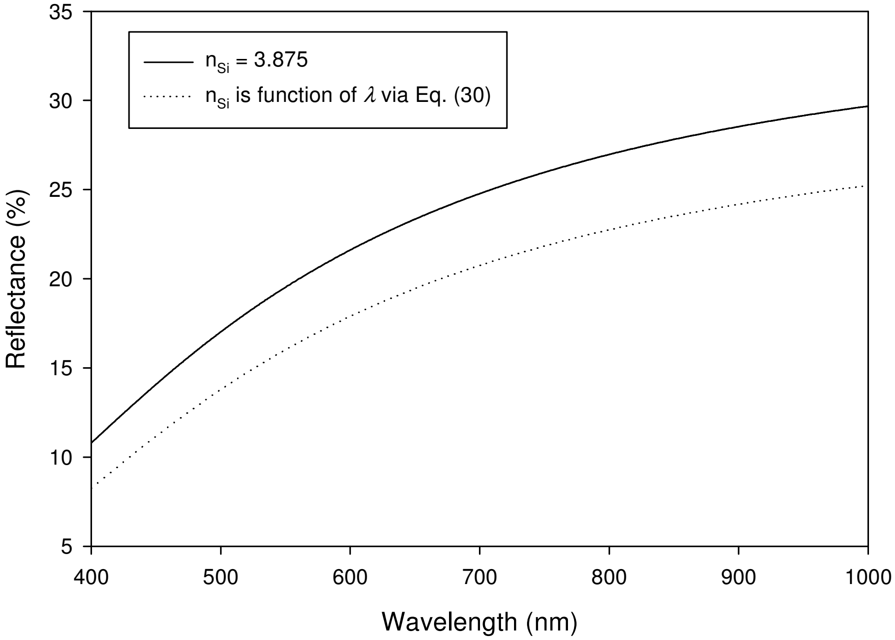

Figure 2.3: The spectral reflectivity of Si_3N_4 SWS for *h* = 68 nm and *s* = 20 nm with constant Si refractive index and refractive index as a function of lambda given by Eq. (28).

Using the above empirical fitted formula, the refractive index of silicon is plotted for wavelength from 400 nm to 1000 nm as shown in Figure 2.4.

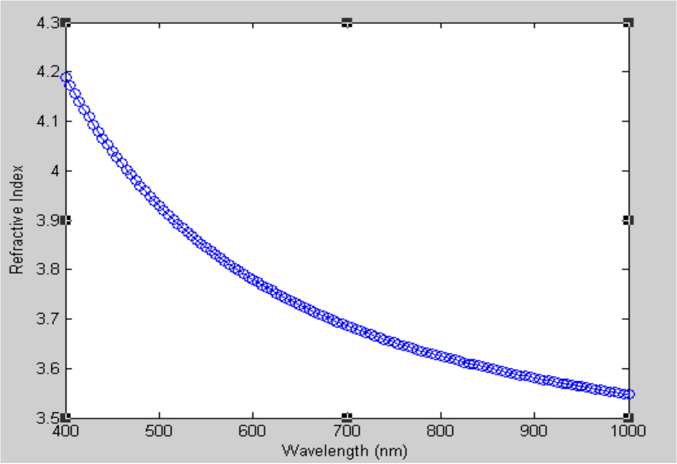

Figure 2.4: Refractive index of Si vs wavelength using equation (28)

Instead of considering the reflectance for a certain wavelength, an effective reflectance is further computed for the structures over a range of the wavelength of incident sunlight. By taking purely Si in the SWS part of Figure 2.1(a), where s = 0 nm and h is designed as a varying factor, we now calculate the effective reflectance R_{eff} [33] for the wavelength λ varying from λ_l = 400 nm to λ_u =1000 nm and compare it with Si_3N_4 SWS. R_{eff} is evaluated by

$$R_{eff} = \frac{\int_{\lambda_l}^{\lambda_u} \frac{R(\lambda)SI(\lambda)}{E(\lambda)} d\lambda}{\int_{\lambda_l}^{\lambda_u} \frac{SI(\lambda)}{E(\lambda)} d\lambda}, \tag{31}$$

where, SI(λ)is spectral irradiance given by ATMG173 AM1.5G reference [34], E(λ) is photon energy and R(λ) is the calculated reflection.

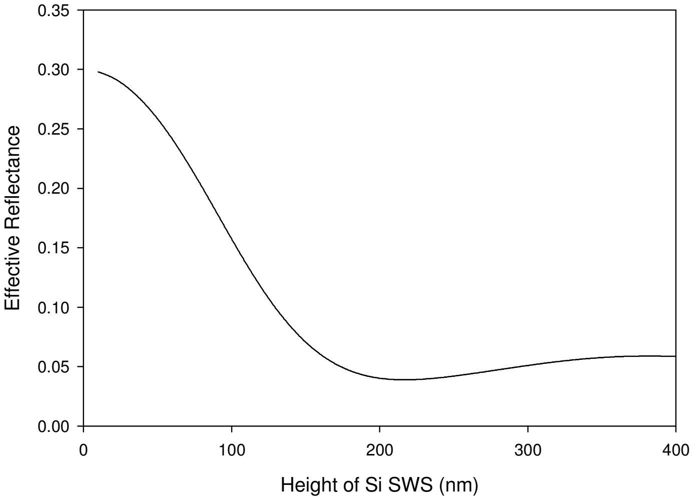

(a)

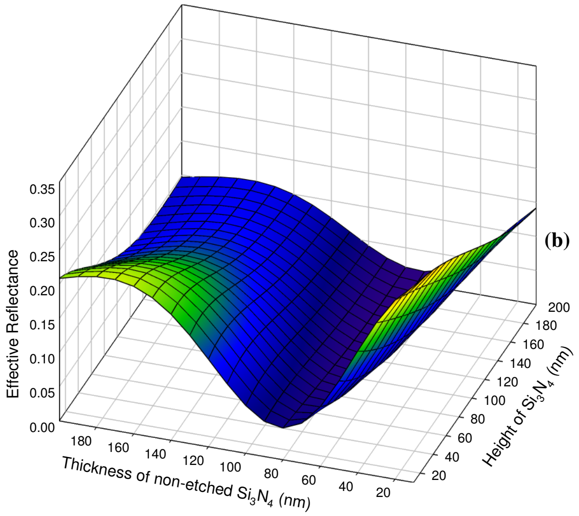

(b)

Figure 2.5: The effective reflectance for the wavelength varying from 400 nm to 1000 nm; plot is as a function of (a) *h* for Si SWS and (b) of *h* and *s* for Si_3N_4 SWS.

Figures 2.5(a) and 2.5(b) show the effective reflectance as a function of h for Si SWS, and of *h* and *s* for Si_3N_4 SWS. For Si SWS, there is a minimum R_{eff} = 3.89% for *h* = 220 nm, and for Si_3N_4 SWS, the minimum of R_{eff} = 3.43% occurs at h = 150 nm and s = 70 nm. Compared with Si SWS, the improvement of R_{eff} for Si_3N_4 SWS is due to the nature of Si_3N_4 and an optimal combination of the height of etched part of Si_3N_4 and the thickness of non-etched part of Si_3N_4.

It has been reported that SLAR and DLAR were used in solar cell, for a unified comparison; similarly, we further examine their R_{eff} over the same wavelength, as shown in Figs. 2.6(a) and 2.6(b).

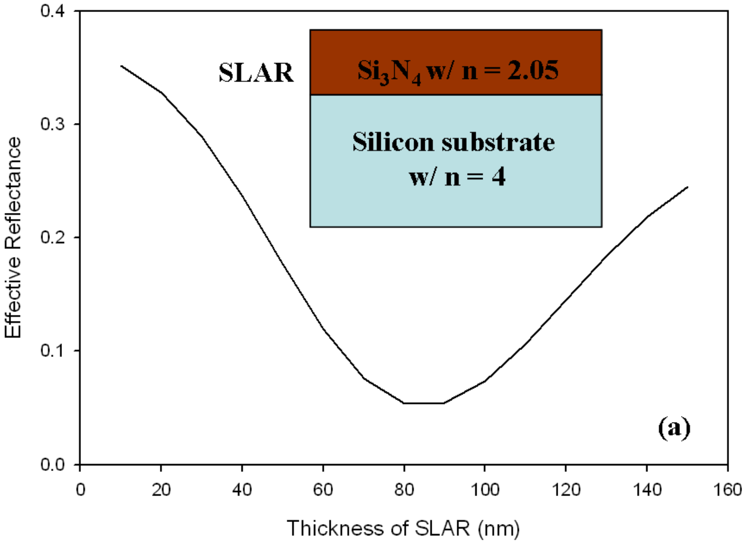

(a)

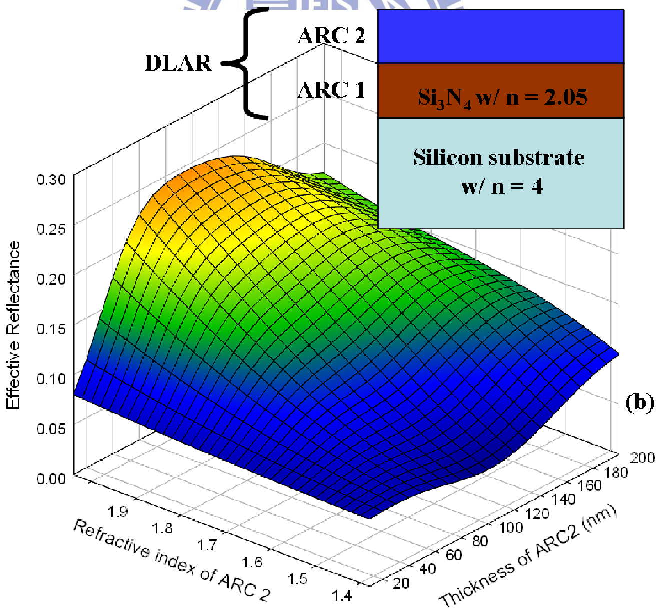

(b)

Figure 2.6: Plot of the effective reflectance for the wavelength varying from 400 nm to 1000 nm. (a) is the result as a function of the thickness of Si_3N_4 ARC

with n = 2.05 for SLAR coating on Si. (b) is the result as a function of the thickness of ARC 2 and refractive index of ARC 2 for Si_3N_4 / ARC 2 DLAR coating on Si. The thickness of Si_3N_4 ARC 1 is fixed at 80 nm which is optimized from (a).

For Si_3N_4 SLAR coating on Si, as shown in the inset of Figure 2.6(a), the refractive index is equal to 2.05, where the thickness of ARC is varied. For Si_3N_4 / ARC 2 DLAR coating on Si, the thickness of ARC 2 and the refractive index of ARC 2 are varied. Note that the thickness of ARC 1 equals 80 nm, as shown in the inset of Figure 2.6(b), directly comes from the optimal value of Figure 2.6(a), and the lower bound of refractive index of ARC 2 starts from 1.38 which is the refractive index of MgF_2. The lowest R_{eff} occurs when the refractive index of ARC 2 is 1.38 and its thickness is 100 nm.

Based upon the investigation of Figs. 2.5 and 2.6, we show the optimal reflectance spectra among the bulk Si (i.e., the bare Si), the optimized SLAR, DLAR, Si SWS and Si_3N_4 SWS for the wavelength from 400 nm to 1000 nm in Figure 2.7.

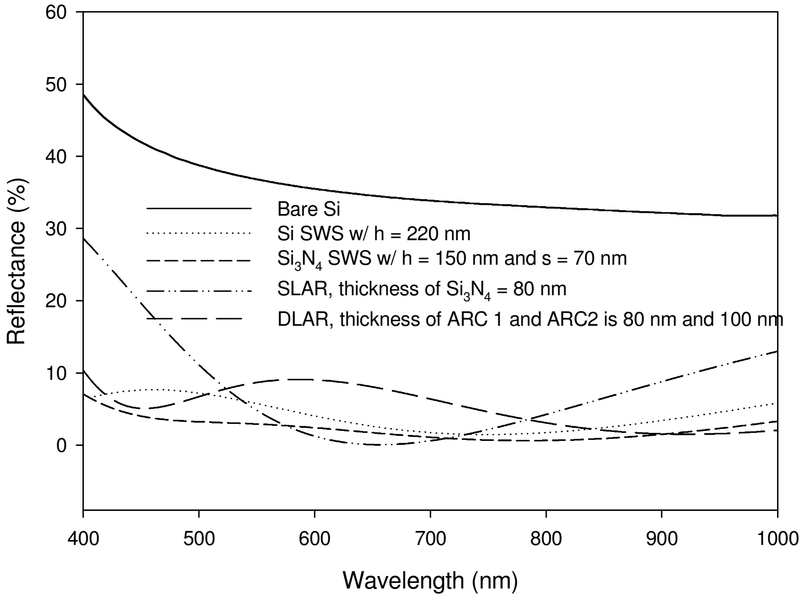

Figure 2.7: Comparison of the reflectance spectra among the bulk Si (i.e., the bare Si), the optimized SLAR, DLAR, Si SWS and Si_3N_4 SWS for the wavelength from 400 nm to 1000 nm.

Table 1 lists the effective reflectivity for those optimized structures of 150 nm Si_3N_4 SWS and 70 nm non-textured Si_3N_4 film, compared with the Si SWS, Si_3N_4 SLAR (its thickness is 80 nm) and Si_3N_4 / MgF_2 DLAR (its thickness is 80 nm / 100 nm) structures. The flat silicon substrate exhibits high reflection > 35% for visible and near infrared wavelengths, Si_3N_4 SLAR coatings exhibits low reflection < 20% for long wavelengths 700 nm and high reflection > 35% for shorter wavelengths 400 nm, and Si_3N_4 / MgF_2 DLAR coatings exhibits low reflection < 10% for long wavelengths 700 nm and high reflection > 20% for short wavelength 400 nm, while the SWS gratings show reduced reflection of < 10% for whole wavelengths. The Si_3N_4 SWS with h = 150 nm and s = 70 nm exhibits lowest effective reflectivity among five structures; consequently, the optimized morphology of Si_3N_4 SWS could be a promising alternative for DLAR in Si solar cell technology.

Table 1. Effective reflectivity for those optimized structures of 150 nm Si_3N_4 SWS and 70 nm non-textured Si_3N_4 film, compared with the Si SWS, Si_3N_4 SLAR (its thickness is 80 nm) and Si_3N_4 / magnesium fluoride DLAR (its thickness is 80 nm / 100 nm) structures.

ARC structure	R_{eff} (%) for λ = 400 nm ~ 1000 nm
Si_3N_4 SWS	3.43
Si SWS	3.89
DLAR	5.39
SLAR	5.41

2.2 Shape Effect

2.2.1 Simulation Procedure

The shape of the SWS may be somewhat variable and, therefore, we performed reflectance calculations for a few model shapes, a cone, paraboloid and cylindrical, respectively as shown in Fig. 2.8, assuming a hexagonal nipple lattice.

The RCWA model as described in section 2.1 was used to calculate the reflectance of the three types of shapes for normally incident light. Therefore, for a cone shape, the equation (16) and (17) will become

$$f\left(z_l\right)=\frac{\pi r_l^2}{\sqrt{3}D^2} \tag{32}$$

$$r_l = r\left(1-\frac{z_l}{h}\right) \tag{33}$$

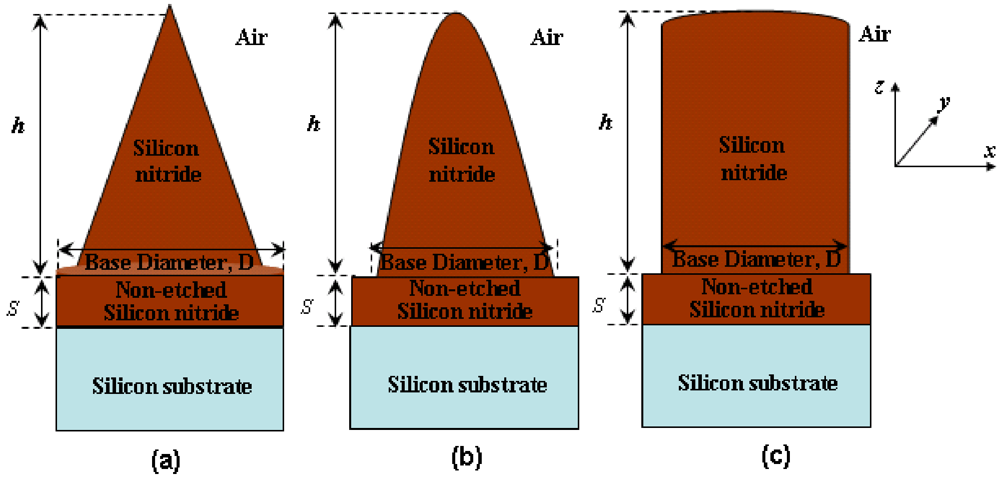

Figure 2.8: Three model shape types (a) cone (b) parabola and (c) cylinder shape.

Similarly, for paraboloid and cylindrical shape, the fraction of Si_3N_4 layer and base width of each layer will be given by equation (34) and (35) respectively.

$$f\left(z_l\right)=\frac{\pi r_l^2}{\sqrt{3}D^2}$$
$$r_l=r\sqrt{\left(1-\frac{z_l}{h}\right)} \tag{34}$$

$$f\left(z_l\right)=\frac{\pi r_l^2}{\sqrt{3}D^2}$$
$$r_l=r \tag{35}$$

2.2.2 Results and Discussion

The calculated effective refractive index at λ = 600 nm from the top of the SWS to the bottom of Si_3N_4 SWS for the four shapes (i.e. Pyramid, parabolic, cone and cylinder) in our simulation is shown in Fig.2.9.

The graded index, which is desirable for suppressing the optical reflection, [35] is observed for pyramid, cone and parabolic shapes—the refractive index changes from 1.0 to 1.5 for pyramid, from 1.0 to 1.4 for cone and from 1.0 to 1.4 at the air/silicon nitride interface and then changes sharply to the bulk index of silicon nitride. But for a cylinder shaped SWS, the effective refractive index calculated is 1.4. From the comparison, it is found that the slope of the change of refractive index is lowest for cone shaped SWS. Using microwave models, experimentally it has been demonstrated that the strong reflectance reduction by a nipple array with cone-shaped nipples [36]. So it is believed that cone shaped Si_3N_4 SWS will give the lowest reflectance compared to pyramid or parabolic or cylinder shaped SWS. The optimizations of the structures and the comparison results will be discussed next.

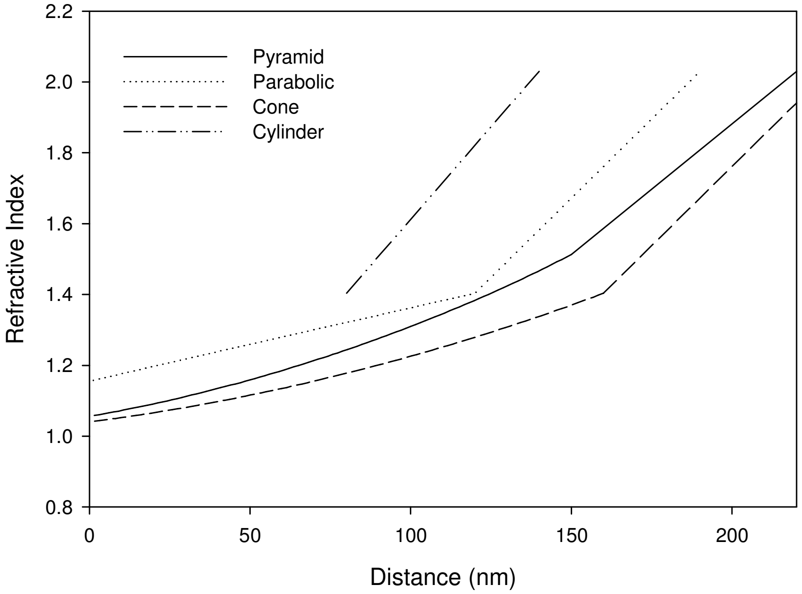

Figure 2.9: Comparison of the change of calculated effective refractive index at $\lambda = 600$ nm from the top of the SWS to the bottom of Si_3N_4 SWS

Similarly, as we varied the "*s*" and "*h*" for pyramid structure, we varied the these two parameters for parabola, cone and cylindrical shapes to see the lowest effective reflectance and the optimization results are shown in Fig. 2.10, Fig. 2.11 and Fig. 2.12, respectively. The reflectance spectra of the optimized structures are compared in Fig. 2.13. The lowest effective reflectance of 3.14% has been seen for the optimized cone shaped SWS as compared to pyramid, parabola and cylinder shape structure.

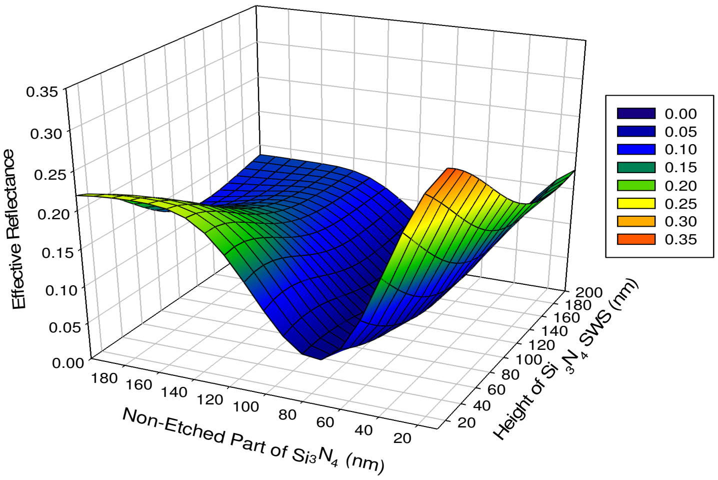

Figure 2.10: Parabola Shape optimization

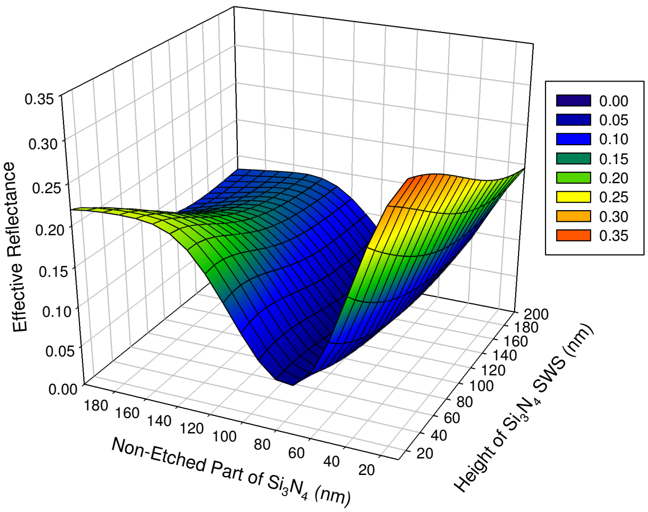

Figure 2.11: Cone Shape Optimization

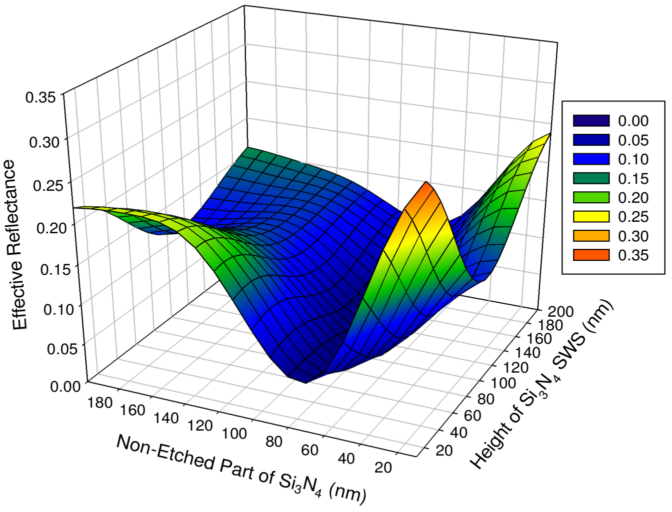

Figure 2.12: Cylinder shape optimization

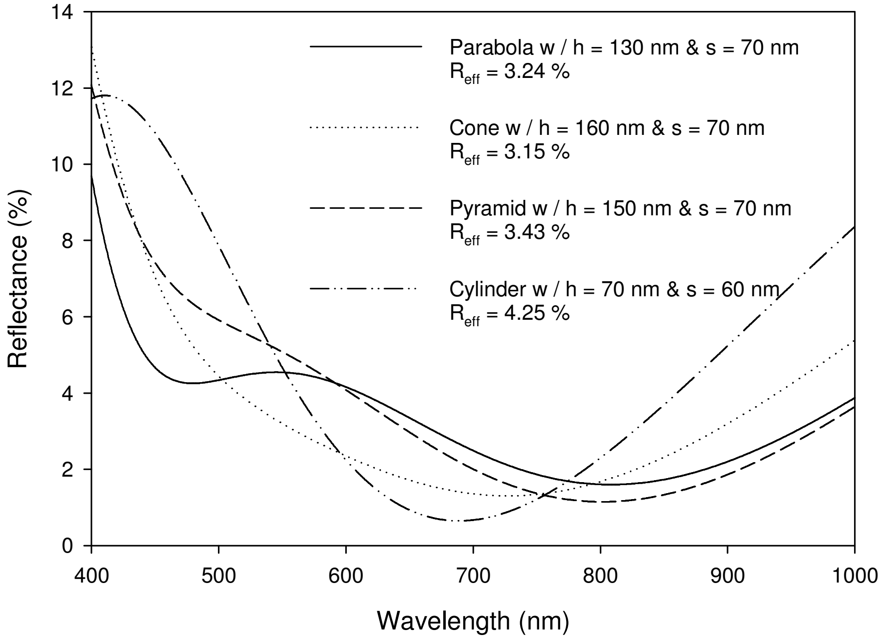

Figure 2.13: Comparison of optimized structures with different shape

But, the comparison of the reflectance spectra of the four shapes as shown in Fig. 2.13 may not be correct as the volumes of the different shapes are different. For this reason, we keep the volume constant for all the shapes and varied the height and base width or base diameter of the SWS to see the effect in reflectance. Note that when we changed the SWS height and base width or base diameter, the thickness of the non-etched Si_3N_4 SWS was kept constant at 70 nm. The effective reflectance of the pyramid, cylinder, parabola, and cone shaped Si_3N_4 SWS with different volume are shown in Fig. 2.14. For the volume from 1×10^5 nm^3 to 1×10^6 nm^3 we found the cone-shaped SWS had the lowest and cylinder-shaped SWS had the highest effective reflectance as compared to other shaped SWSs.

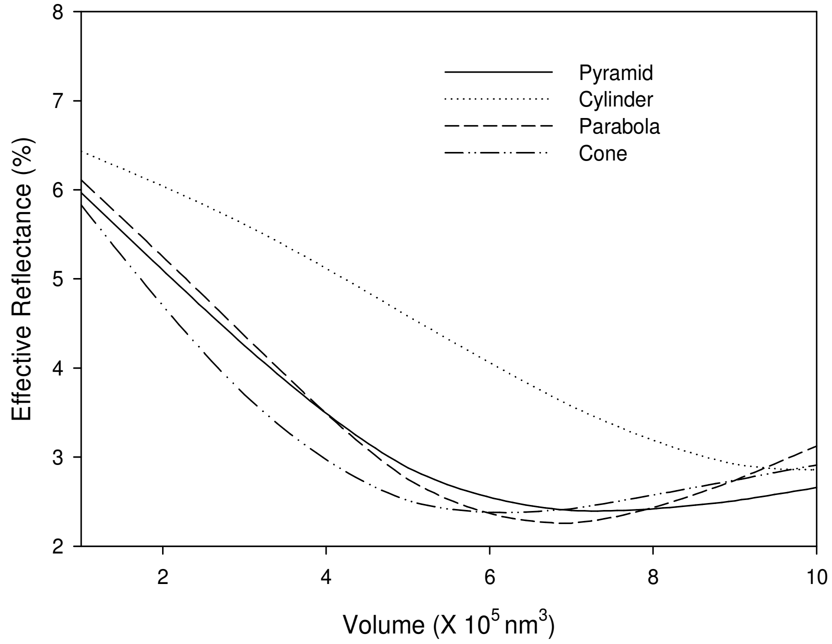

Figure 2.14: The effective reflectance of Si_3N_4 SWS versus the SWS volume.

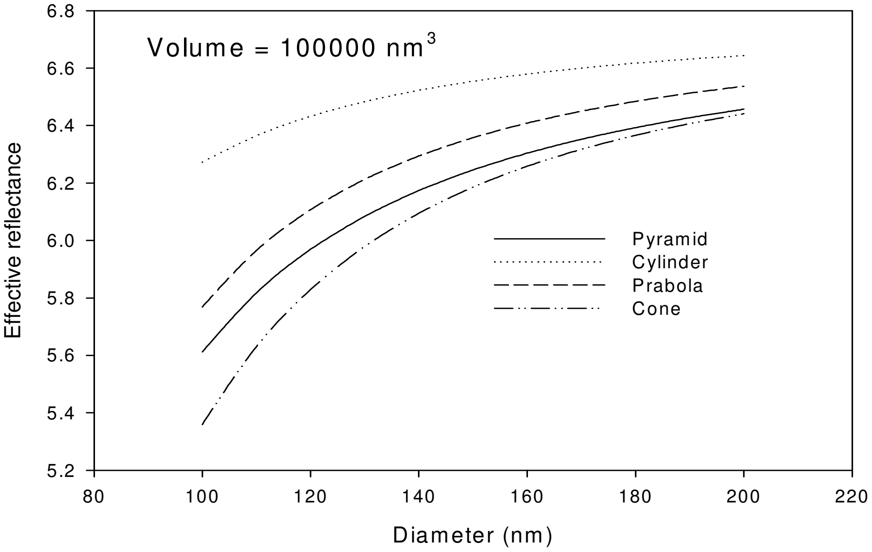

Volume = 100000 nm^3
Effective reflectance
Diameter (nm)
6.8
6.6
6.4
6.2
6.0
5.8
5.6
5.4
5.2
80
100
120
140
160
180
200
220
Pyramid
Cylinder
Prabola
Cone

(a)

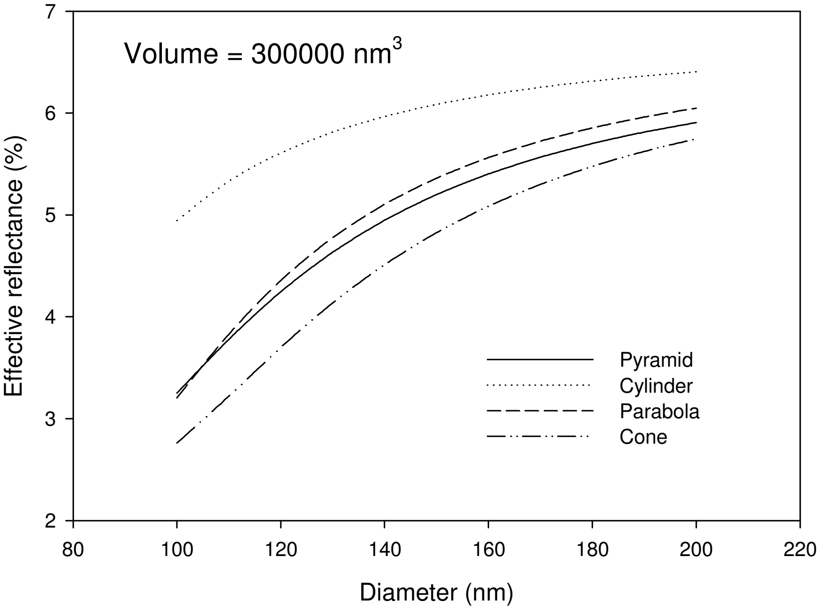

Volume = 300000 nm^3
Effective reflectance (%)
Diameter (nm)
7
6
5
4
3
2
80
100
120
140
160
180
200
220
Pyramid
Cylinder
Parabola
Cone

(b)

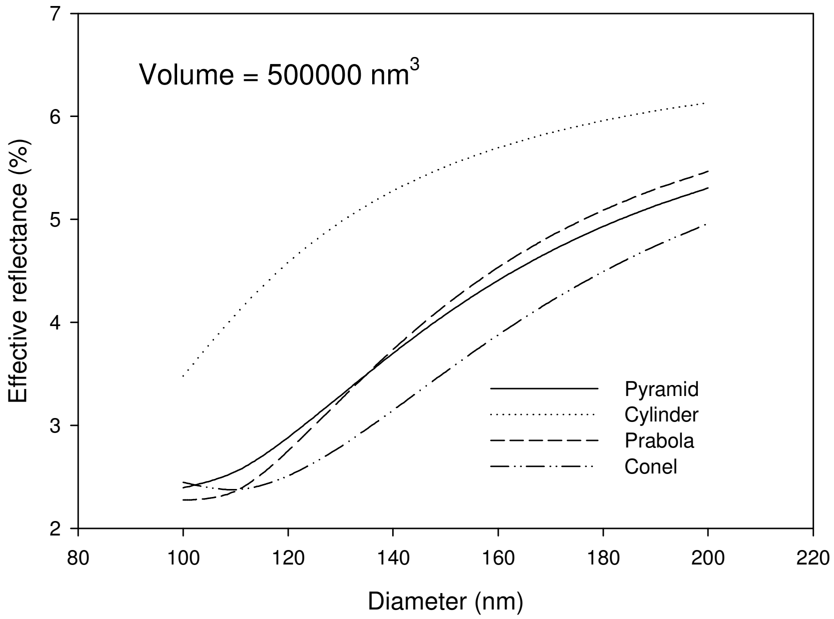

(c)

Figure 2.15: Effective reflectance Vs Base diameter w / volume (a) 100000 nm^3 (b) 300000 nm^3 and (c) 500000 nm^3.

2.3 The Electrical Characteristics Calculation

To get the electrical data for the solar cell with Si_3N_4 SWS, the simulated reflectance of the optimized Si_3N_4 SWS and single-layer anti-reflection (SLAR) structures are post-processed using PC1D program. In this section, we will introduce about the PC1D software and describe the simulation procedure for the calculation of solar characteristics.

2.3.1 Introduction to PC1D software

PC1D is the simulation program in most widespread use among the photovoltaic community. It is a software package for personal computers that uses finite-element analysis to solve the fully-coupled two-carrier semiconductor transport equations in one dimension. This program is particularly useful for analyzing the performance of optoelectronic devices such as solar cells, but can be applied to any bipolar device whose carrier flows are primarily one-dimensional. flexible internal models make it. It is easy to set up and modify a broad range of one-dimensional problems from MOS capacitors to bipolar transistors. Heterojunctions, arbitrary doping profiles, doping-dependent mobility, bandgap narrowing, Auger recombination, interface recombination, temperature effects, photogeneration of carriers, complex boundary conditions, and transient solutions are some of the powerful features built into this program [37].

The development of this program was initiated by Dr. Paul A. Basore while he was a member of the faculty of electrical engineering at Iowa State University in 1984, with funding from the photovoltaic technology division of Sandia National Laboratories. The project was originally intended to take advantage of the interactive environment of personal computers to help analyze solar cells. Additional funding from IBM Corporation in the form of a Faculty Development Award made it possible to expand the program into a full-featured semiconductor analysis package for public distribution. Later it was developed at UNSW, Australia [38] and distributed freely.

2.3.2 Simulation Procedure

To calculate the solar cell electrical characteristics before measuring realistic silicon solar cells, we have used the measured reflectance spectra and simulated reflectance spectra as the input of the PC1D program. Performance of optical system directly affects the short-circuit current density (J_{SC}) and the conversion efficiency of a solar cell. The short circuit current density and open circuit voltage of the solar cell were calculated under the standard AM1.5 global spectrum from its IV characteristics. Then, η of a solar cell is deduced out of the three photovoltaic parameters: V_{oc}, short-circuit current (I_{sc}) and fill factor (FF) and is given by:

$$\eta = FF \frac{I_{SC} V_{OC}}{P_I}, \tag{36}$$

where, P_I designates the incident power ($P_I = 0.1\ W/cm^2$ under illumination AM1.5 G) and

$$FF = \frac{P_{\max}}{I_{SC} V_{OC}}, \tag{37}$$

Spectrally resolved internal quantum efficiency (IQE) is calculated by making two wavelength scans of the cell [39]. In the first scan, the cells spectral response (SR) is determined by dividing the short-circuit current at each wavelength by the light power incident on the cell. In the second scan, the cell's reflectance (*R*) is calculated as a function of wavelength. The reflected light is integrated over the full hemisphere, including both light reflected directly off the front surface of the cell and the light that has entered the cell, reflected off the back surface, and subsequently escaped. The external quantum efficiency (EQE) is then calculated using

$$EQE = 1 - SR\left[\frac{\left(hc/\lambda\right)}{q\left(1-R\right)}\right], \tag{38}$$

where, λ is the free-space wavelength and q is the elementary unit of charge.

2.3.3 Simulation Settings

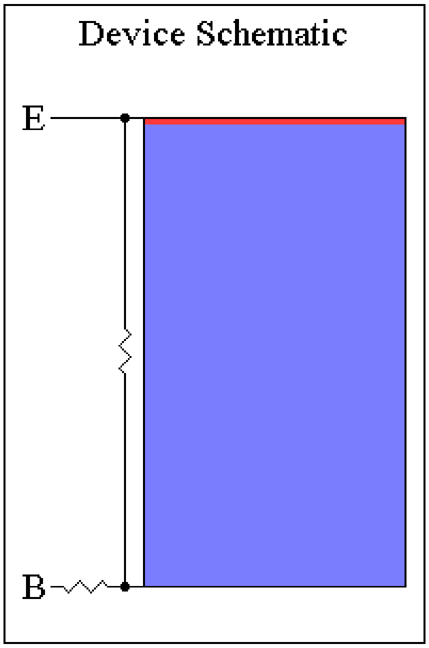

Figure 2.16 Device Schematic used in PC1D for solar characteristics calculation.

The device schematic used for solar characteristics study is as shown in Fig. 2.16. In this calculation, thickness of the whole region is set to 300 μm with material p-type Si. The p-type Si is set with resistively of 1.008 Ω-cm and a diffused emitter with error function distribution, where the emitter sheet resistance is 99.4 Ω / sq. The emitter diffusion is done with n-type impurity and peak concentration of $6 \times 10^{19}/\text{cm}^3$. The base contact resistance is 0.015 Ω and the cell's internal shunt conductance is 0.3 Siemens. The bulk life time of Si was set to 7.03 μs, where the front and back surface recombination velocity is 1800 cm / s and 25 cm / s, respectively [40].

2.3.4 Results and Discussion

Electrical characteristics and the external quantum efficiency obtained from PC1D simulation for a Si solar cell using the reflectance spectra for the three explored structures described in chapter 2, they are Si_3N_4 SWS, SLAR and DLAR are further conducted as shown in Fig. 5.2.

It is clear that J_{SC} and V_{OC} of Si_3N_4 SWS are higher than those of Si_3N_4 SLAR and Si_3N_4 / MgF_2 DLAR structures, as seen from Fig. 2.17(a). A clear increase in efficiency of 1% can be seen for silicon solar cell with Si_3N_4 SWS over a cell with single layer Si_3N_4 ARCs and 0.71% higher in efficiency than the DLAR coated solar cell, which is due to lower reflectance of DLAR to Si_3N_4 SWS over the longer wavelength region that leads to lower short circuit current.

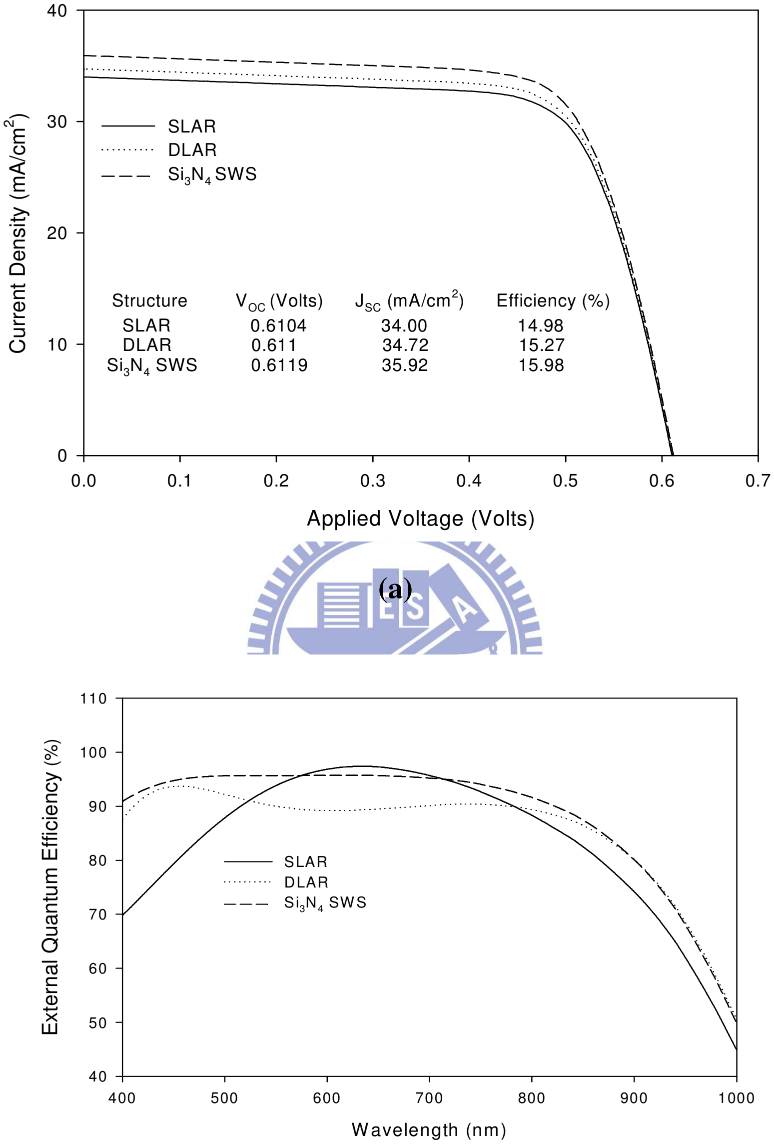

Structure	V_{OC} (Volts)	J_{SC} (mA/cm^2)	Efficiency (%)
SLAR	0.6104	34.00	14.98
DLAR	0.611	34.72	15.27
Si_3N_4 SWS	0.6119	35.92	15.98

(a)

(b)

Figure 2.17: (a) Electrical characteristics and (b) the external quantum efficiency obtained from PC1D simulation for a silicon solar cell using the reflectance spectra for the three optimized structures, they are Si_3N_4 SWS, SLAR and DLAR.

With solar cells, the external quantum efficiency is often measured, which could be calculated by the current obtained outside the device per incoming photon. As shown in Fig. 2.17(b), the calculated external quantum efficiency also confirms the higher efficiency of the designed Si_3N_4 SWS compared with the others.

2.4 Summary

In this Chapter, we have presented preliminary results of designed silicon nitride sub-wavelength structures. Using the results of rigorous coupled wave analysis simulation for the pyramidal-shaped silicon nitride sub-wavelength structures, the ratio of silicon nitride sub-wavelength structures height and non-textured part of silicon nitride has been optimized. The reflectance results for the optimized sub-wavelength structures have been compared in terms of effective reflectivity. Then lowest effective reflectivity sub-wavelength structures were compared with previously optimized 80nm Si_3N_4 SLAR and 80 nm / 100 nm Si_3N_4 / MgF_2 DLAR. A low effective reflectivity of 3.43% can be obtained for a silicon nitride SWS height and non-etched layer of 150 nm and 70 nm respectively, which is less than 80 nm Si_3N_4 SLAR of 5.41% and comparable with Si_3N_4 / MgF_2 DLAR of 5.39%.

From the study of different shaped Si_3N_4 SWS, the cone shaped SWS shows the lowest effective reflectance for same volume as compared to pyramid, cylinder and parabola shaped Si_3N_4 SWSs.

From the PC1D simulation result, 1% cell efficiency increase is observed for the optimized Si solar cell with Si_3N_4 SWS, compared with the cell with single layer Si_3N_4 antireflection coatings (ARCs); furthermore, compared with DLAR coated solar cell, the increase is about 0.71%. The improvement on the cell efficiency is mainly due to lower reflectance of Si_3N_4 SWS over a wavelength region from 400 nm to 600 nm that leads to lower short circuit current.

Therefore, there is a need to study more about fabrication of silicon nitride sub-wavelength structure to improve the solar cell efficiency with a single layer ARCs which is believed to reduce the reflectance and improve the passivation properties of silicon solar cell.

Chapter 3

Fabrication Processes and Measurements

In this chapter, we describe the fabrication process for silicon nitride SWS. The method to control the size and density of nickel nano clusters that can work as the mask for etching the Si_3N_4 film and the effect of inductively coupled plasma (ICP) etching time on the height of fabricated Si_3N_4 SWS will be discussed. The process condition is empirically optimized to make the lowest average reflectance in the wavelength region 400 nm to 1000 nm. The measured reflectivity of the fabricated Si_3N_4 SWS is further compared with the simulated results for accuracy verification. Also, the measured reflectance of fabricated Si_3N_4 SWS will be compared and discussed with measured reflectance of SLAR and DLAR coatings in this chapter.

3.1 Sub-wavelength structure Fabrication Process

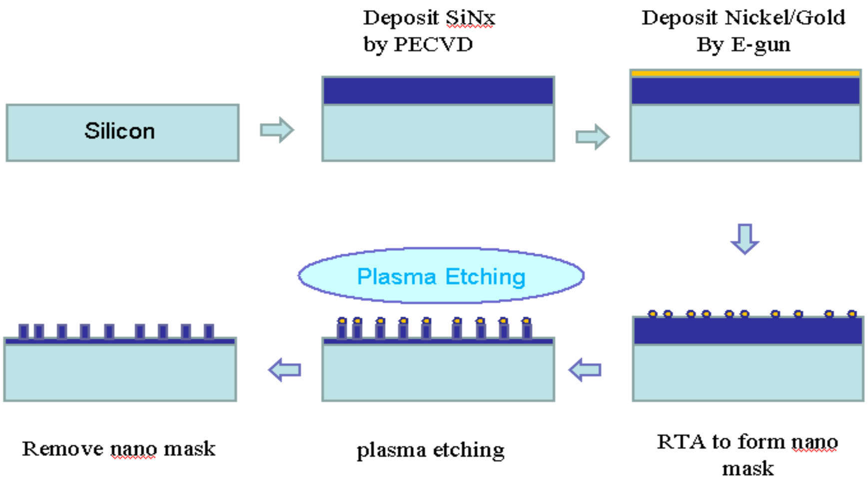

Figure 3.1 SWS fabrication process

The fabrication process of the silicon nitride SWS in this study includes:

1. Wafer clean
2. Deposition of silicon nitride
3. Nano-mask formation
    - Deposition of metal film
    - Rapid Thermal Anneal
4. Inductively Coupled Plasma (ICP) Etching
5. Nano-mask removal

The detail will be described in the following sections.

3.1.1 Wafer Clean

To remove the native oxide from the wafer, the first step in the SWS fabrication was the wafer cleaning. A p-type (111) silicon wafer was used for SWS fabrication process. First, wafer was dipped into ACE for 5 minutes and then dipped into IPA for 5 minutes followed by nitrogen blow.

3.1.2 Deposition of Silicon Nitride

Plasma enhanced chemical vapor deposition (PECVD) technique has been used to deposit silicon nitride. PECVD is an excellent alternative for depositing a variety of thin films at lower temperatures than those utilized in CVD reactors without settling for a lesser film quality. For example, high quality silicon dioxide films can be deposited at 300 to 350 degrees centigrade while CVD requires temperatures in the range of 650 to 850 degrees centigrade to produce similar quality films.

PECVD uses electrical energy to generate a glow discharge (plasma) in which the energy is transferred into a gas mixture. This transforms the gas mixture into reactive radicals, ions, neutral atoms and molecules, and other highly excited species. These atomic and molecular fragments interact with a substrate and, depending on the nature of these interactions, either etching or deposition processes occur at the substrate. Since the formation of the reactive and energetic species in the gas phase occurs by collision in the gas phase, the substrate can be maintained at a low temperature. Hence, film formation can occur on substrates at a lower temperature than is possible in the conventional CVD process, which is a major advantage of PECVD.

Some of the desirable properties of PECVD films are good adhesion, low pinhole density, good step coverage, and uniformity.

For silicon nitride deposition, two gases silane (SiH_4) and ammonia (NH_3) has been used with nitrogen (N_2) as carrier gas in the PECVD machine (STS 300 PC series-310PC) situated in compound semiconductor device laboratory (CSDLab) as shown in Figure 3.2.

The reaction mechanisms are shown below:

$$\begin{aligned} SiH_4 + NH_3 &\longrightarrow SiN:H + 3H_2 \\ SiH_4 + N_2 &\longrightarrow SiN:H + 3H_2 \end{aligned} \qquad \textbf{(39)}$$

Figure 3.2 CSD Lab PECVD machine

The deposition conditions for our silicon nitride deposition using PECVD are listed in Table 3.1. Carrier gas Nitrogen had a flow rate of 1960 sccm during silicon nitride deposition. The index of refraction (n) of the films was measured with N & K analyzer 1280 using a wavelength of 633 nm, which is placed in National Nano-Device Laboratory (NDL), Taiwan.

Table 2 Deposition Condition for Silicon Nitride by PECVD

SiH_4 Sccm	NH_3 Sccm	Pressure (Pa)	Power (Watt)	Temp. (^oC)	Time (Min.)	Thickness (A^0)	Refractive index (n)
55	55	900	20	300	33	2000	2.1 @6328A^0

3.1.3 Nano-mask Formation

Nano-mask formation was carried out by two steps. First a metal film of gold or nickel was deposited on silicon nitride surface using e-gun evaporator (*ULVAC E-560*) and then followed by a rapid thermal anneal (RTA) process (*AG Associates Heatpulse 610 RTA system*) to form self-assembled metal nano-masks on the silicon nitride surface.

- **Deposition of Metal**

It is known that the initial thickness of the metal film can play an important role in determining surface morphology at a given temperature [15, 16]. So, we obtain four samples with different initial thickness of nickel film and the initial nickel thicknesses are (20 ± 0.05) nm in sample-1, (15 ± 0.05) nm in sample-2, (08 ± 0.05) nm in sample-3 and (3 ± 0.05) nm in sample-4.

- **Rapid Thermal Anneal**

Rapid thermal anneal (RTA) is a process used in semiconductor device fabrication which consists of heating a single wafer at a time in order to affect is electrical properties. Unique heat treatments are designed for different effects. Wafers can be heated in order to activate dopants, change film-to-film or film-to-wafer substrate interfaces, density deposited films, change states of grown films, repair damage from ion implantation, move dopants or drive dopants from one film into another or from a film into the wafer substrate. Rapid thermal anneals are performed by equipment that heats a single wafer at a time using lamp based heating that a wafer is brought near. Unlike furnace anneals they are short in duration, processing each wafer in several minutes. Rapid thermal anneal is a subset of processes called rapid thermal processing (RTP), which refers to a semiconductor manufacturing process which heats silicon wafers to high temperature (up to 1200 ^{o}C or greater) on a timescale of several seconds or less. The wafers must be brought down (temperature) slow enough however, so they do not break due to thermal shock.

The sample-1, sample-2, sample-3 and sample-4 are proceeded in the rapid thermal annealing (RTA) under the mixture of forming gas of H_2 & N_2 (*90 % & 5%*) with a flow rate of 3 sccm at 850°C for 60 seconds and pressure of 100 Pa, and then we form nickel nano clusters, which can serve as the etch masks for silicon nitride. The RTA process is shown in Figure 3.3. The cluster morphology of the samples is studied by the scanning electron micrograph (SEM), as will be described later in chapter 4.

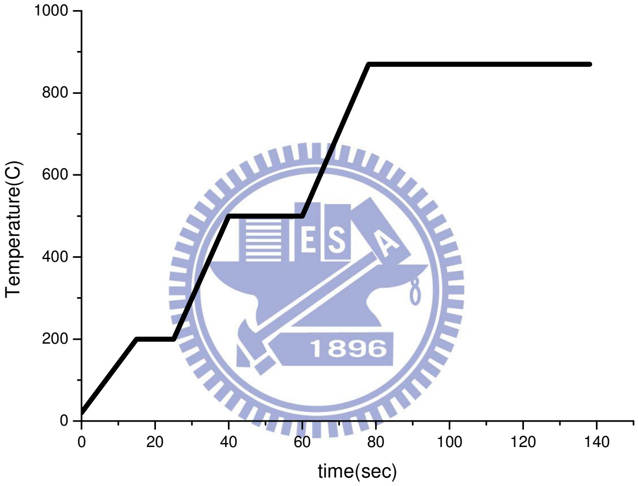

Figure 3.3 Rapid Thermal Anneal Process graph

3.1.4 Inductively Coupled Plasma (ICP) Etching

The samples are etched by ICP etcher (ULVAC NE 550) with bias power of 200 watt, process pressure 1Pa, and antenna power of 100W, using different gases and etching parameters which will be discussed in results and discussion section.

3.1.5 Nano-mask Removal

To remove the residual nickel mask, the sample was dipped into pure nitric acid

(HNO_3) solution for 5 min at room temperature followed by de-ionized (DI) water rinse.

3.2 Characterization Methods

3.2.1 Morphology Analysis

The morphology of sub-wavelength structures was analyzed by Scanning electron microscope (Hitachi - 4700). A few nanometer of Pt was deposited on the SWS to increase the resolution as silicon nitride is a dielectric material.

3.2.2 Reflectance Measurement

The reflectance of the SWS were measured using an n&k analyzer (model: 1280, N&K Tech. Inc.). Deuterium and tungsten lamp were used in this instrument, which can provide the reflectance for the wavelength range from 190 nm to 1000 nm. The angle of incidence was 4^0 for the measurement.

3.3 Results and Discussion

3.3.1 Process optimization of Nanomask for silicon nitride SWS

3.3.1.1 RTA temperature optimization

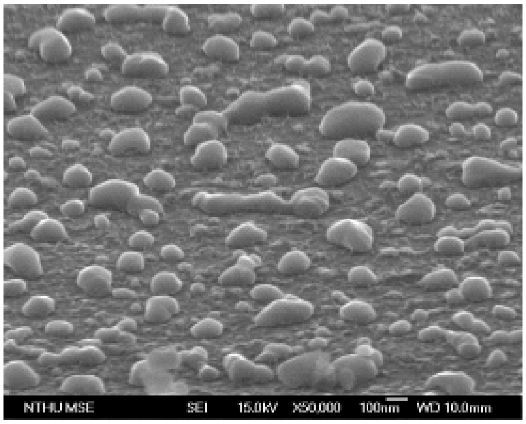

(a)

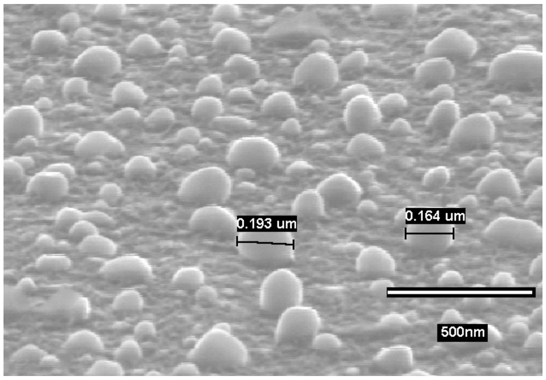

(b)

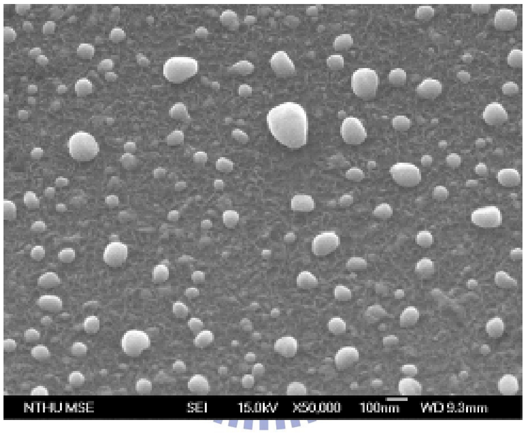

(c)

Figure 3.4: SEM Images of nickel nano-clusters formed after RTA for 60 sec at (a) 800 °C (b) 850 °C (c) 900 °C.

Three different temperatures has been tried for nano mask formation on silicon nitride using nickel as metal film. The SEM image of the Sample-1 after RTA for 60 sec at 800°C, 850°C, and 900°C are shown in Figs. 3.4(a), 3.4(b), and 3.4(c) respectively. From Fig. 3.4(a), it can be seen that the nano clusters are not formed properly. Nano clusters are formed perfectly for RTA for 850°C and 900°C as seen from Figures 3.4(b) and 3.4(c). But, the densities of the nanoclusters are higher for the sample annealed at 850°C than the sample annealed at 900°C. Therefore we chose the RTA temperature 850°C for 60 sec as the best condition for nickel nano cluster formation for the rest of our study.

3.4.1.2 Initial Nickel Thickness optimization

Figures 3.5(a), 3.5(b), 3.5(c) and 3.5(d) show the SEM images of the nickel nano clusters formed after rapid thermal annealed at 850°C for 60 sec for the Sample-1, Sample-2, Sample-3 and Sample-4 respectively. It is known that the thickness of the Ni film plays an important role in determining Ni nano clusters at a given temperature [41, 42]. The influence of the initial Ni layer thickness on the nano-cluster size after RTA processed at 850°C for 1 min is investigated.

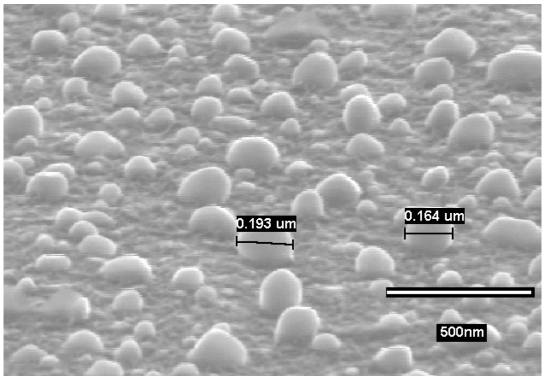

(a)

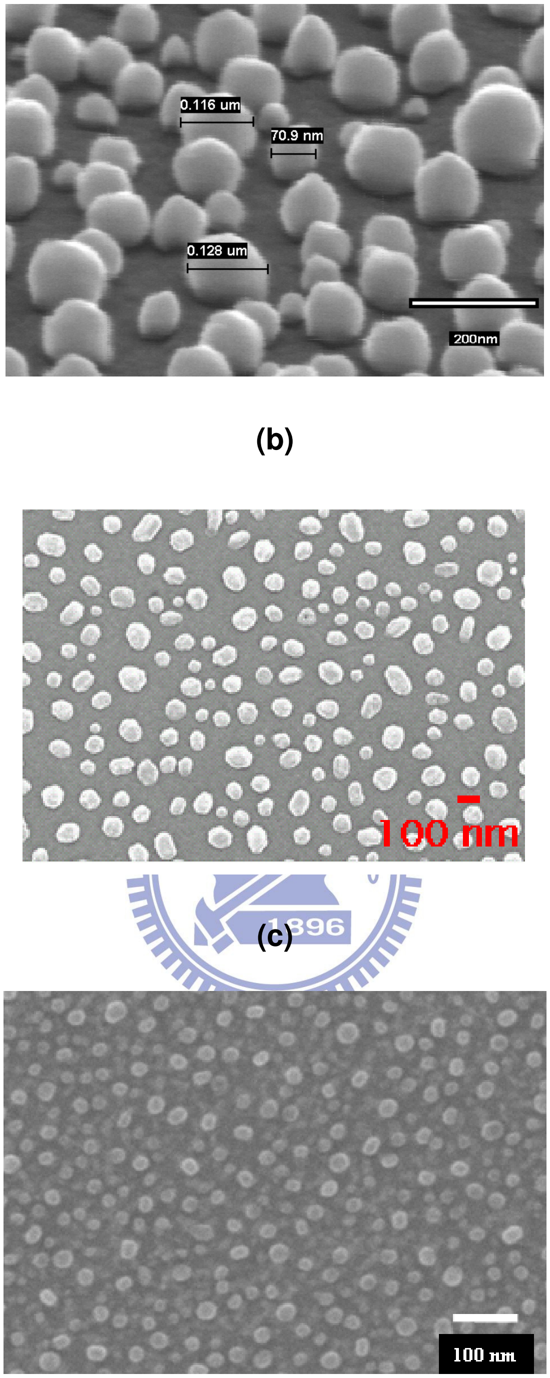

(b)

(c)

(d)

Figure 3.5: SEM Images of nickel nano-clusters formed after RTA at 850 ^{0}C for 60 sec (a) Sample 1 w/ initial nickel thickness 20 nm; (b) Sample 2 w/ initial nickel thickness 15 nm; and (c) Sample 3 w/ initial nickel thickness 8 nm; (d) Sample 4 w/ initial nickel thickness 3 nm.

The diameters of the nano-clusters vary from 160 to 200 nm for Sample-1, from 80 to 130 nm for Sample-2, from 50 to 120 nm for Sample-3 and from 40 to 50 nm for Sample-4.

The effect of initial nickel thickness on density and diameter of the nickel nano-clusters is shown in Fig. 3.6. From, Fig. 3.6, we observe that the dimension of Ni nano clusters decreases and the density of nickel nano clusters increases when the thickness of the deposited nickel film decreases from 20 nm to 3 nm.

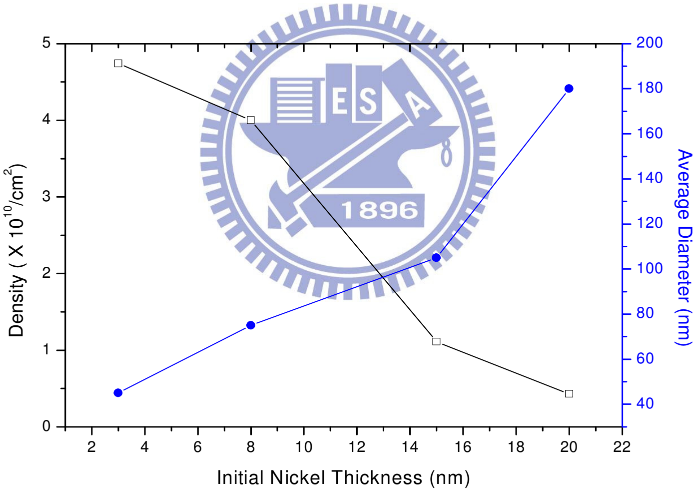

Figure 3.6: Effect of initial nickel thickness on density and average diameter of the Ni nano-clusters after RTA at 850 ^{o}C for 60 sec.

This is due to the weak interaction between the Ni and the silicon nitride layer for higher initial nickel thickness results in a low activation energy barrier to Ni migration which results in larger islands forming from smaller islands or weakly bound individual Ni atoms [43]. Based on this observation it could be concluded that the dimension and density of the nano-cluster formation can be controlled by the initial thickness of nickel deposited above Si_3N_4 layer.

3.3.2 Height optimization of silicon nitride SWS

Figures 3.7(a), 3.7(b), and 3.7(c) show the SEM image of the fabricated Si_3N_4 SWS on Sample-4 after ICP dry etching for 60 sec, 100 sec and 120 sec.

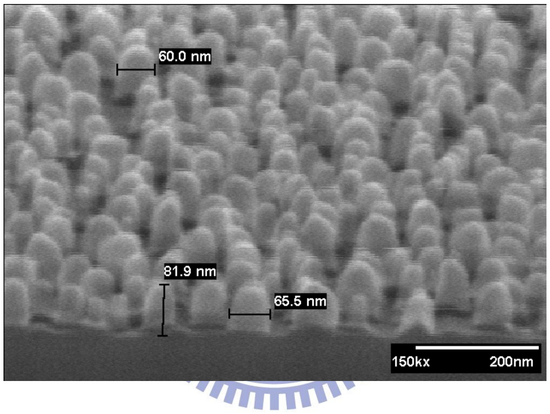

(a)

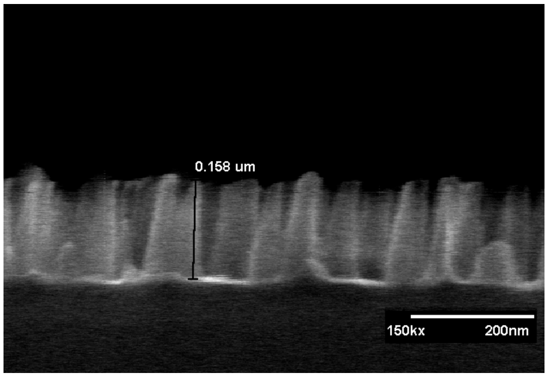

(b)

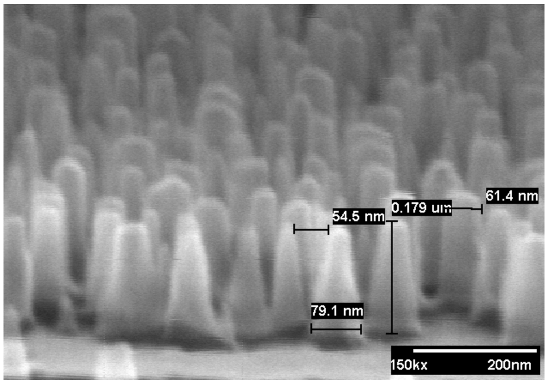

(c)

Figure 3.7: SEM Images of fabricated Si_3N_4 SWS w/ ICP etching time (a) 60 sec; (b) 100 sec; (c) 120 sec for Sample-4.

From Fig. 3.7(a), the height of the silicon nitride SWS is measured to be 70 - 90 nm and tip diameters of fabricated samples of SWS varied from 60 - 70 nm, which are nearly same as that of nickel nano-clusters. Similarly, as shown Fig. 3.7(b) the height of the silicon nitride SWS is measured to be 160 - 170 nm and tip diameters of fabricated SWSs vary from 40 - 60 nm for etching time of 100 sec and the height of the silicon nitride SWS is measured to be 170 - 180 nm and tip diameters of fabricated samples of SWS vary from 50 - 60 nm for etching time of 120 sec as shown in Fig. 3.7(c).

Figure 3.8 shows the curve between average heights of the fabricated Si_3N_4 SWS with ICP etching time.

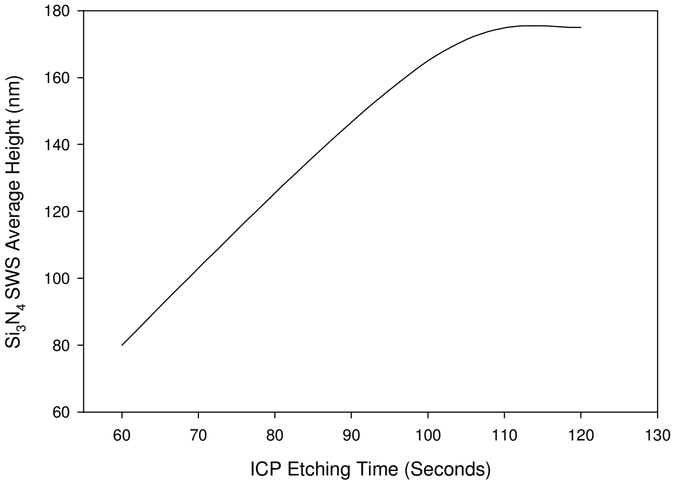

Figure 3.8: Effect of etching time on the average height of fabricated Si_3N_4 SWS.

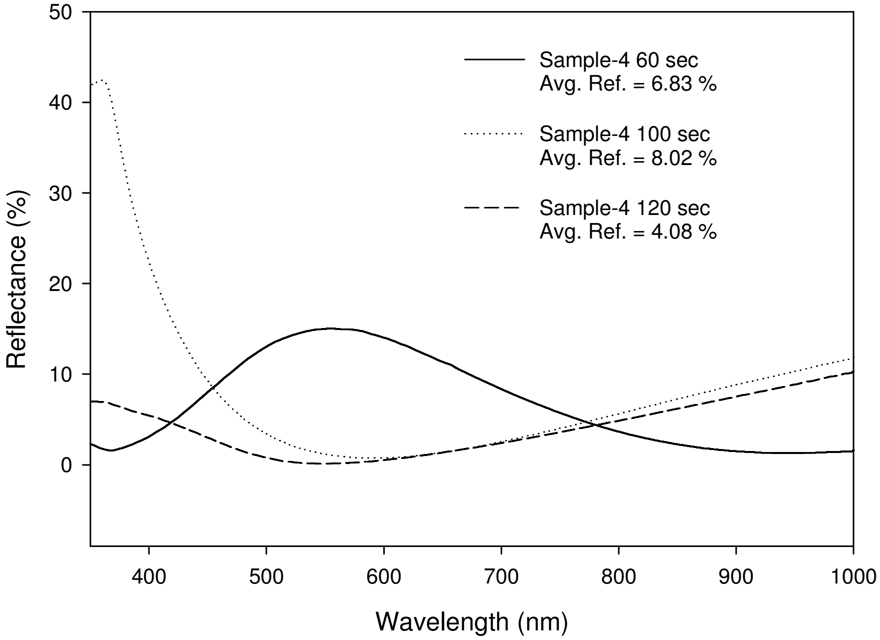

Figure 3.9: Comparison of reflectance spectra for the fabricated Si_3N_4 SWS with different etching time, for Sample-4.

The measured reflectance spectrum for the sample-4 has been compared for different etching times as shown in Fig. 3.9. The calculated average reflectance for the wavelength range from 350 to 1000 nm of all the samples are shown in Fig. 3.9. The average reflectance was calculated by following equation:

$$R_{av} = \frac{1}{\lambda_u - \lambda_l} \int_{\lambda_l}^{\lambda_u} R(\lambda) d\lambda \tag{40}$$

Where $R(\lambda)$ is the reflectance of the design and λ_l & λ_u are the lower and upper wavelength of the design window. We observed the lowest average reflectance of 3.12 % for the Si_3N_4 SWS of sample-4 with ICP etching time of 120 sec and average height of 155 nm.

Figures 3.10(a), 3.10(b), and 3.10(c) show the SEM image of the fabricated Si_3N_4 SWS on Sample-3 after ICP dry etching for 90 sec, 120 sec and 180 sec.

The observed height with etching time for sample-3 is tabulated in Table 2 and the reflectance spectra for different etching time are shown in Fig. 3.11.

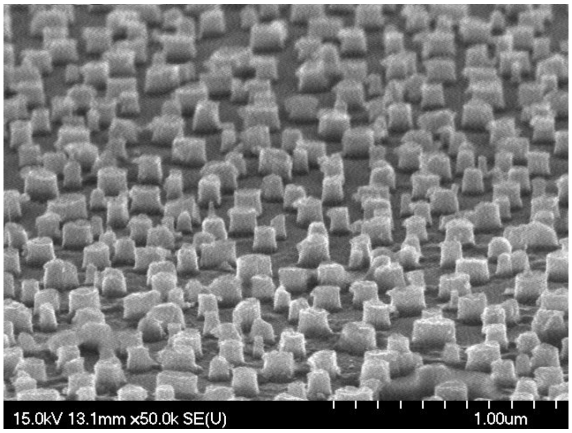

(a)

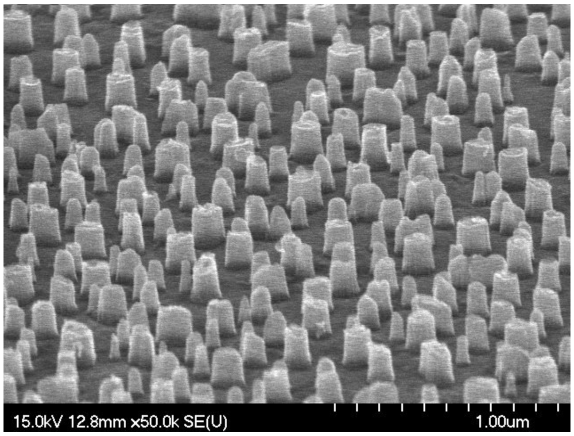

(b)

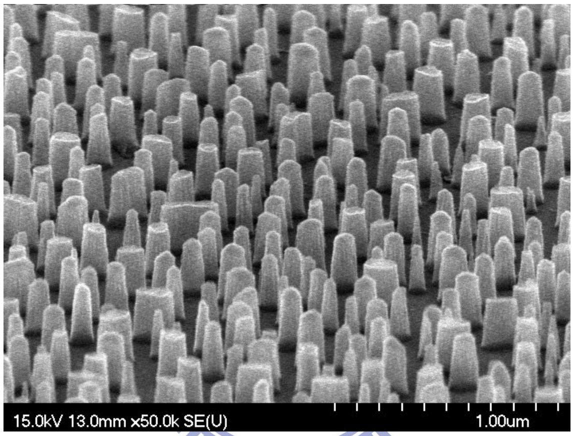

(c)

Figure 3.10: SEM Images of fabricated Si_3N_4 SWS w/ ICP etching time (a) 90 sec; (b) 120 sec; (c) 180 sec for Sample-3.

Table 3: The height of the fabricated Si_3N_4 SWS with different etching time, for Sample-3.

CF_4 / O_2 etching time (s)	**Height (nm)**
90	**111**
120	**153**
180	**230**

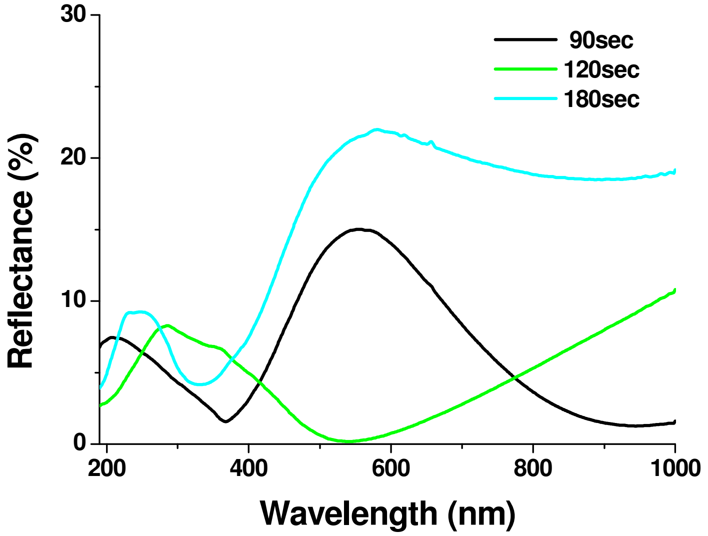

Figure 3.11: Comparison of reflectance spectra for the fabricated Si_3N_4 SWS with different etching time, for Sample-3.

Fig. 3.12 shows the SEM image of the fabricated Si_3N_4 SWS on Sample-2 after ICP dry etching for 120 sec.

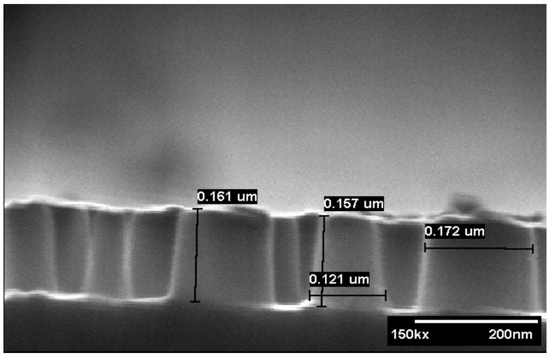

Figure 3.12: SEM Image of fabricated Si_3N_4 SWS w/ ICP etching time 120 sec

From Fig. 3.12, the height of the fabricated SWS is measured to be 150 - 160 nm and the tip diameter of the SWS was measured as 120 - 170 nm.

The reflectance spectra of the sample-3 and sample-4 were compared in Fig. 3.13 for etching time of 120 sec. From this comparison, we got the lowest average reflectance of 3.89% for the sample-3 with average SWS height of 155 nm. Since the average height of the fabricated SWS on Sample 3 is close to our computer simulated results (i.e., the Si_3N_4 SWS with h = 150 nm and s = 70 nm), as shown in Fig. 2.7; therefore, we chose this structure as our target structure for analysis.

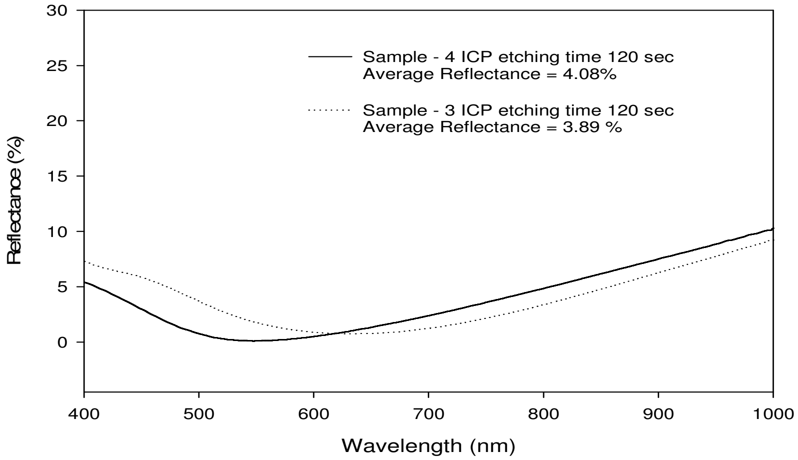

Figure 3.13: Comparison of reflectance spectra of sample-3 and sample-4 for ICP etching time 120 sec, where the average heights of Si_3N_4 SWS were 155 nm and 175 nm, respectively.

3.4 Results Comparison

3.4.1 Comparison of measurement and simulation

Fig. 3.14 shows the measured reflectance compared with the simulated reflectance for the Si_3N_4 SWS of the height 155 nm and the non-etched Si_3N_4 thickness of 65 nm. The non-etched Si_3N_4 thickness was assumed to be 65 nm because the total thickness of Si_3N_4 deposited in the fabricated sample was 220 nm.

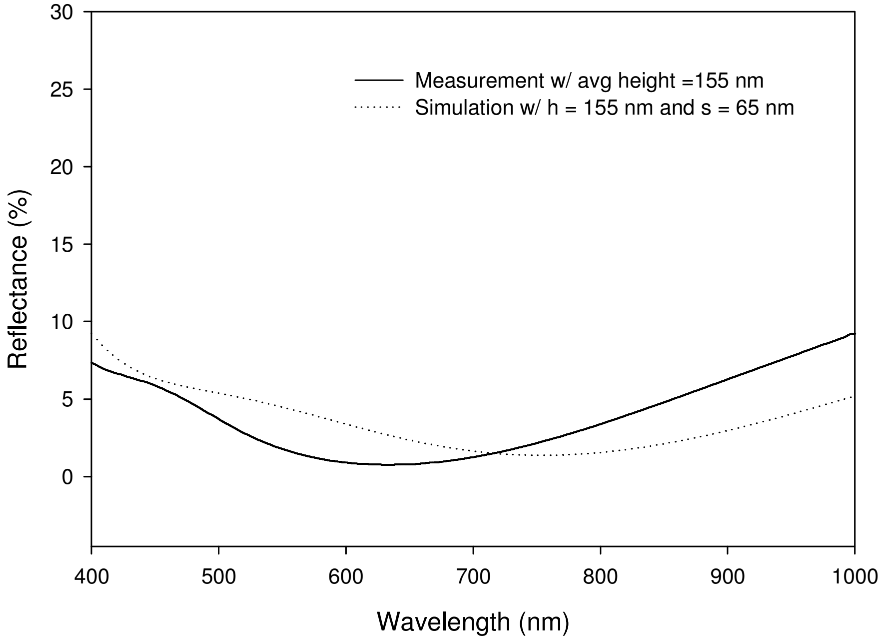

Figure 3.14: Comparison of fabricated Si_3N_4 SWS with Simulated Si_3N_4 SWS w/ *h* = 155 nm and *s* = 65 nm, for the wavelength range from 400 nm to 1000 nm.

The results are around the upper bound and lower bound of the reflectance spectra (they are within 5% variation for both cases) for the wavelength ranging from 400 nm to 1000 nm. The differences between the simulated and measured results, as shown in Fig. 3.14, are due to the non-uniform nature of the fabricated Si_3N_4 SWS, whereas, the simulation was merely done for a periodic nature of the SWS. Notably the shape of the simulated structure was different from the shape of the fabricated structure, which is believed to be the one of the reason for the difference in the simulated and fabricated reflectance spectra.

3.4.2 SWS Comparison with SLAR & DLAR

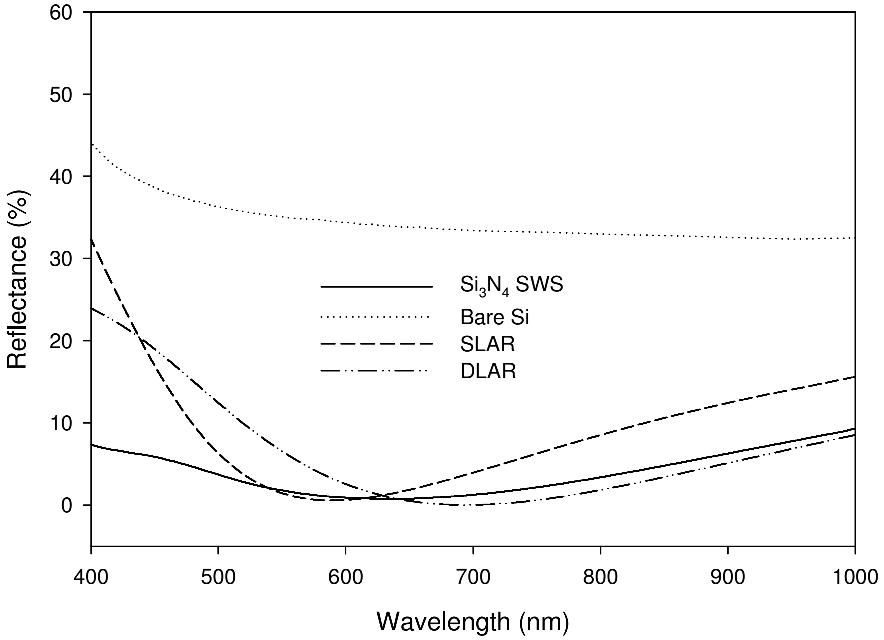

Figure 3.15: Comparison of the reflectance spectra among the bulk Si (i.e., the bare Si), the optimized SLAR, DLAR, and Si_3N_4 SWS for the wavelength from 400 nm to 1000 nm.

Figure 3.15 shows the comparison of the measured reflectivity from a polished silicon wafer with 69.1 nm silicon nitride SLAR coating and fabricated silicon nitride SWS on silicon wafer. The flat silicon substrate exhibits high reflection > 35% for visible and near infrared wavelengths, silicon nitride SLAR coatings exhibits low reflection < 20% for long wavelengths 700 nm and high reflection > 35% for shorter wavelengths 400nm, and silicon nitride/MgF_2 DLAR coatings exhibits low reflection < 10% for long wavelengths 700 nm and high reflection > 20% for short wavelength 400 nm, while the SWS gratings show reduced reflection of < 10% for long wavelengths 700 nm and shorter wavelengths 400nm. The reflection is further reduced to < 1% for wavelengths around 580 nm ~ 680nm. The silicon nitride SWS gratings exhibit lower reflection than colloid-based antireflection coatings on crystalline silicon solar cells [44], other SWS ARCs made by lithographic techniques with typical reflection of ~2%-10%, [45-48]. Additionally, optimization of the height and non-etched part of silicon nitride of SWS will facilitate further improvement of the antireflection performance.

. The average reflectance for the wavelength range from 400 nm to 1000 nm for a bare Si, SLAR w/ Si_3N_4 thickness of 69.1 nm, DLAR of Si_3N_4 / MgF_2 w/ thickness of 69.1 nm and 56 nm respectively for Si_3N_4 & MgF_2 and fabricated Si_3N_4 SWS are shown in Table 3. From Table 3 it is clear that the silicon nitride SWS have the lowest average residual reflectance of 3.89 % as compared to bare silicon, 69.1 nm silicon nitride SLAR coatings and DLAR coating with 69.1 nm silicon nitride & 56 nm MgF_2 .

Table 4: Average residual reflectivity calculated by the equation (37) for measured reflectance of bare silicon, 69.1 nm silicon nitride deposited on silicon, 69.1 nm silicon nitride & 56 nm MgF_2 double layer deposited on silicon and 140 ~ 160 nm silicon nitride SWS fabricated on silicon.

Structure	Average Reflectance (%)
Silicon	34.43
Silicon nitride SLARC*	8.79
Silicon nitride / MgF_2 DLARC**	6.21
Silicon nitride SWS***	3.89

*SLARC-Single Layer Anti-reflective Coating

**DLARC-Double Layer Anti-reflective Coating

** SWS- Sub-wavelength Structure

3.5 Summary

It is observed that the height of the SWS could be controlled with the dry etching time. Meanwhile, the density and the diameter of SWS could be controlled with the dimension of the nano cluster formed after RTA. From the above observations, it could be concluded that the non-periodic Si_3N_4 SWSs can be fabricated using the proposed technique.

We observed the lowest average reflectance of 3.89 % for the Si_3N_4 SWS of sample-3 with ICP etching time of 120 sec and average height of 155 nm. Therefore, For the consideration of working wavelength region of silicon-based solar cells, the SWS with height of 140 - 160 nm is suitable as the antireflective structure and believed to increase the solar cell performance as compared to solar cell w/ SLAR structure.

Chapter 4

Fabrication of Nanocones

In this chapter, we have studied the effect of ICP conditions on the profile of fabricated sub-wavelength structure on Silicon nitride antireflection coating layers. We have fabricated the silicon nitride nanocone structures using the self assembled nickel nanoclusters followed by inductively coupled plasma (ICP) etching on silicon substrate and explore the reflection properties of the texturing structures through spectroscopic measurements. In this chapter, we have explained the fabrication of nanopillars and nanocones on silicon nitride using one step and two step ICP etching methods, respectively and compared the reflection properties of the texturing structures with different morphologies.

4.1 Experimental

First of all the polished (100) silicon was cleaned with dilute HF to remove the native oxide. A layer of 300 nm thick silicon nitride (Si_3N_4) was then deposited on a polished (100) silicon wafer by plasma enhanced chemical vapor deposition (PECVD) technique. A nickel film with a thickness of 5 nm was then evaporated on the silicon nitride surface using an E-beam evaporating system. The nickel film was then rapid thermal annealed (RTA) under the forming gas (mixture of H_2 and N_2) with a flow rate of 3 sccm at 850°C for 60 s to form nickelclusters, which served as the etch masks for silicon nitride. Initial nickel thickness of 5 nm has been chosen to get the higher density and smaller dimension of Ni nano-clusters in our experiment. The sample was then etched by ICP etcher (ULVAC NE 550) using different gases and etching parameters which will be discussed in results and discussion section. To remove the residual nickel mask, the sample was dipped into pure nitric acid (HNO_3) solution for 5 min at room temperature. The morphology of SWS was analyzed by Scanning electron micrograph (SEM). The reflectances of the SWS were measured using an N&K 1280 analyzer.

4.2 Results and Discussions

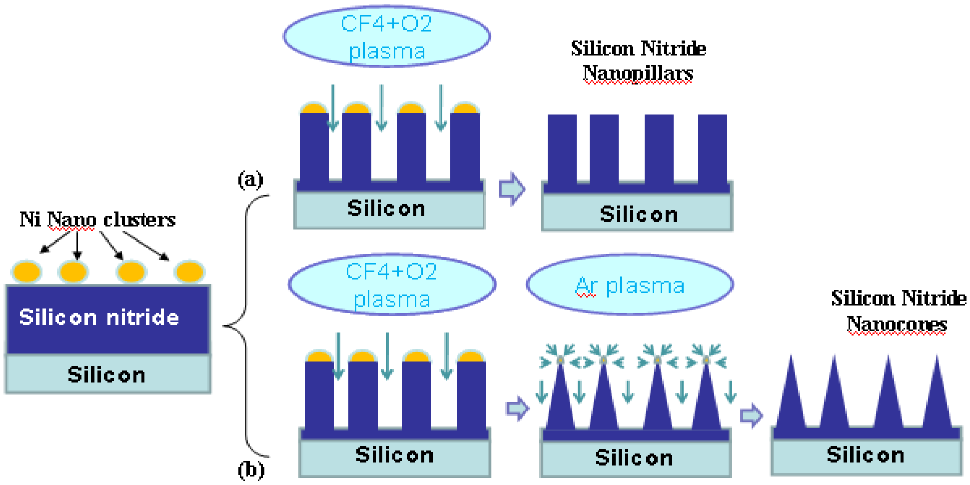

Figure 4.1: Schematic of fabrication process of (a) silicon nitride nanopillars (b) silicon nitride nanocones.

Figure 4.1 shows the schematic illustrations of the fabrication of nanopillars and nanocones by one- and two-step ICP etching processes, respectively. The one-step etching process, which is shown in Fig. 1(a), involved non-etching of nickel nanoclusters, whereas etching of the underlying silicon nitride film. As the size of the nickel nanoclusters was not changed, the etched area of the underlying silicon nitride depends on the diameter of the nano clusters. Thus, silicon nitride pillar structures were readily obtained from the one-step etching process. The two-step etching process as shown in Fig. 4.1(b) involved minifying of nickel nano clusters and etching of the underlying silicon nitride film, gradually. As the size of the nano clusters decreased gradually, the etched area of the underlying silicon nitride increased gradually. Thus, silicon nitride nanocone structures were readily obtained from the two-step etching process. One-step etching process was carried out by using a mixture of CF_4 and O_2 and based on fluorine chemistry. The two-step etching process was carried out by using a mixture of CF_4 and O_2 in first step and followed by the etching with Ar. The mechanism can be confirmed by watching the scanning electron microscope (SEM) image as shown in Fig. 4.2.

The SEM image of the sample etched by Ar gas for 30 s and 120 s were shown in Figs. 4.2(a) and 4.2(b), respectively, after the nanoclusters were formed. From these figures we could see the decrease of nickel nano cluster size after etched in Ar gas for long time, which confirms the mechanism involved to form nanocones described previously. Similarly, we could see the effect of ICP etching using the mixture of CF_4/O_2 gas to form the nanopillars from the Figs. 4.2(c) and 4.2(d).

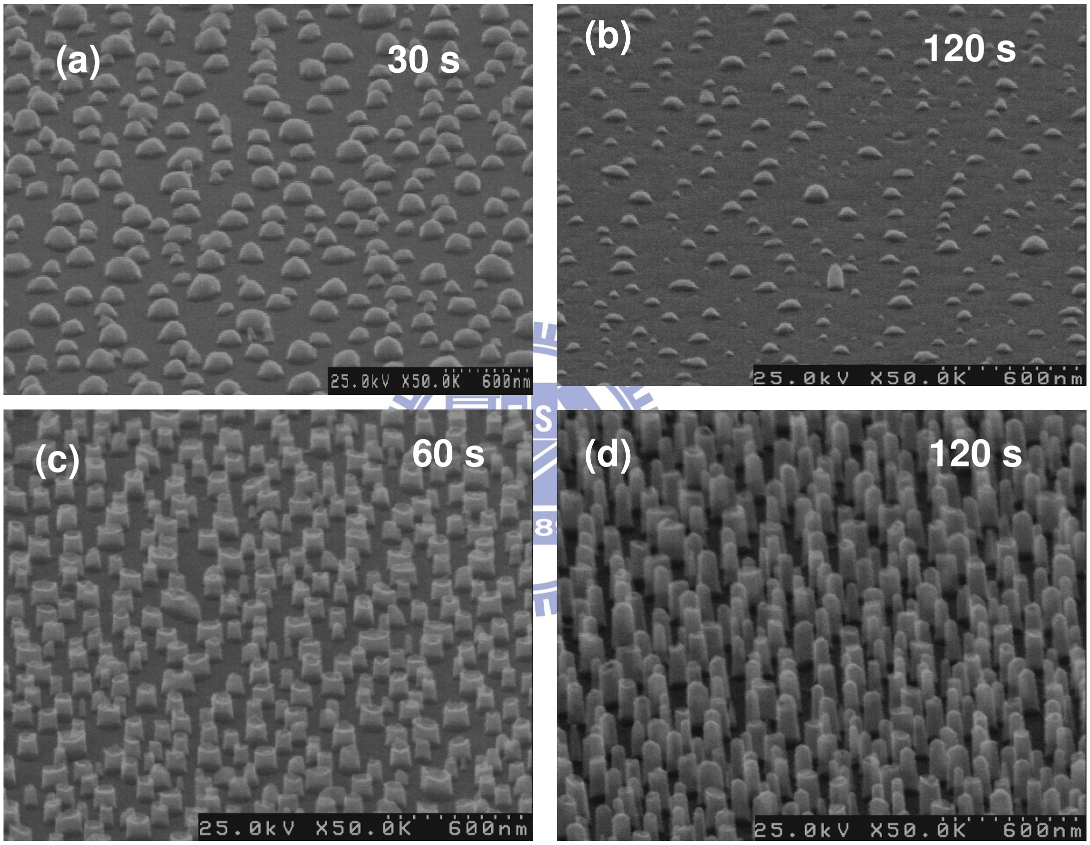

Figure 4.2: SEM images of Ar plasma etching of nickel nano cluster on silicon nitride for (a) 30 s (b) 120 s. SEM images of CF_4/O_2 plasma etching of nickel nano cluster on silicon nitride for (a) 60 s (b) 120 s.

Using the developed method, experiments were performed to demonstrate control over nanopillar and nanocone height and structures. In the first series, samples starting with nickel nano clusters were etched by a gas mixture of CF_4/O_2 to between 100 to 250 nm heights by different etching time. The resulting nanopillars with corresponding heights could be seen in Figs. 4.3(a) - 4.3(d).

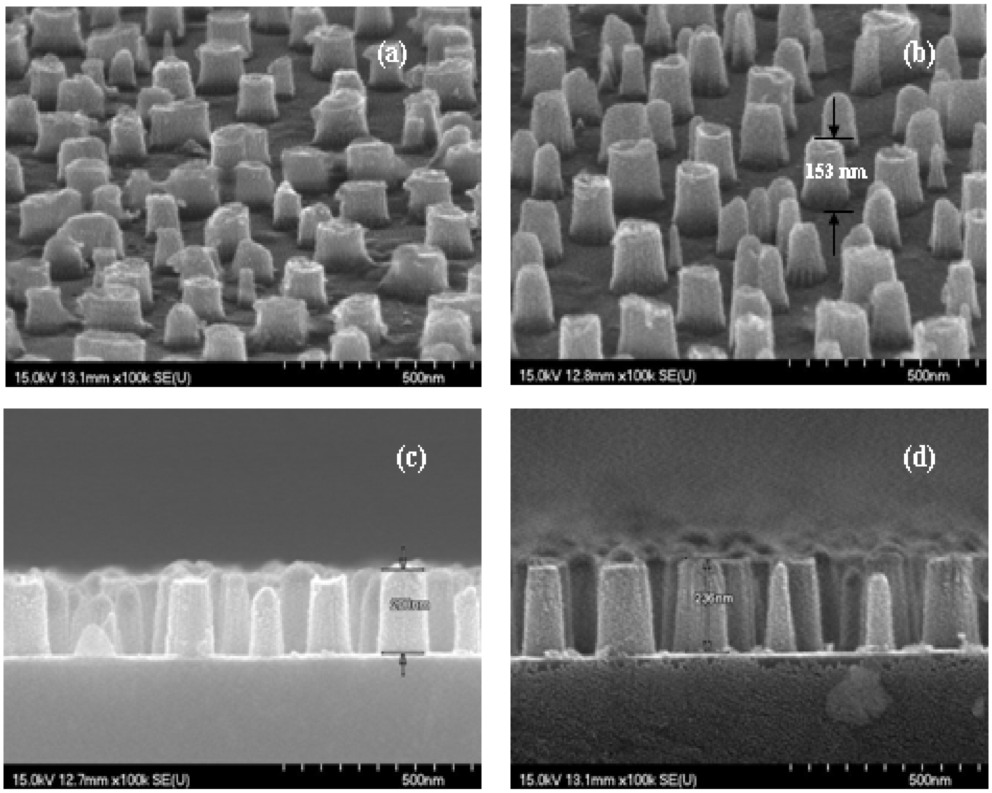

Figure 4.3: SEM images of fabricated nanopillar structures on silicon nitride film using one-step etching process for etching time: (a) 90 s (b) 120 s (c) 150 s (d) 180 s.

Figure 4.3(a) showed nanopillars with height around 110 nm with CF_4/O_2 etching time of 90 s. silicon nitride nanopillars with height around 150 nm has been achieved after etched for 120 s as shown in Fig. 4.3(b). Similarly, Figs. 4.3(c) and 4.3(d) showed the achieved silicon nitride nanopillars with height around 210 and 240 nm for etching time of 150 s and 180 s, respectively.

Figure 4.4 displayed top-view and cross-sectional images of the different nanocones obtained after varying etching time of the CF_4/O_2, but keeping the etching time of Ar constant as 120 s, for the two-step process.

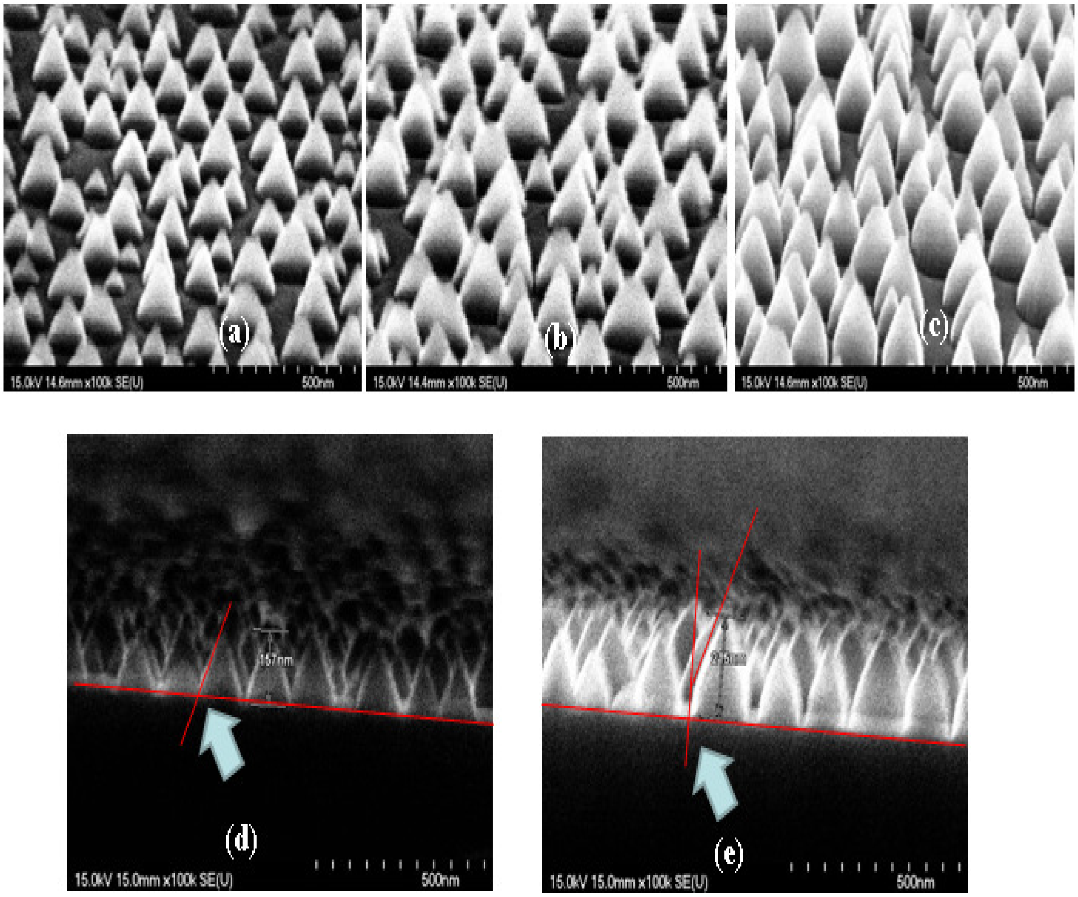

Figure 4.4 : SEM images (top-view) of fabricated nanocone structures on silicon nitride film using two-step etching process for etching time: (a) 90 s (b) 120 s (c) 150 s. Cross-section SEM view of the fabricated nanocone structures with etching time (d) 90 s and (e) 180 s.

Figures 4.4(a) - 4.4(c) showed the top-view of the nanocones fabricated for the etching time of 90 s, 120 s, and 150 s respectively. Figures 4.4(d) and 4.4(e) shows the cross-section view of the structure shown in Fig. 4.4(a) and 4.4(c), which indicated that etched silicon nitride having a height of around 157 nm for the etching time of 90 sec and around 215 nm for the etching time of 150 sec, respectively. Note that in Fig. 4.4(d) and 4.4(e) the base of the nanocones were different from each other, which were clearly seen.

This behavior of the nanocone base could be explained by our proposed possible mechanism as shown in Fig. 4.5.

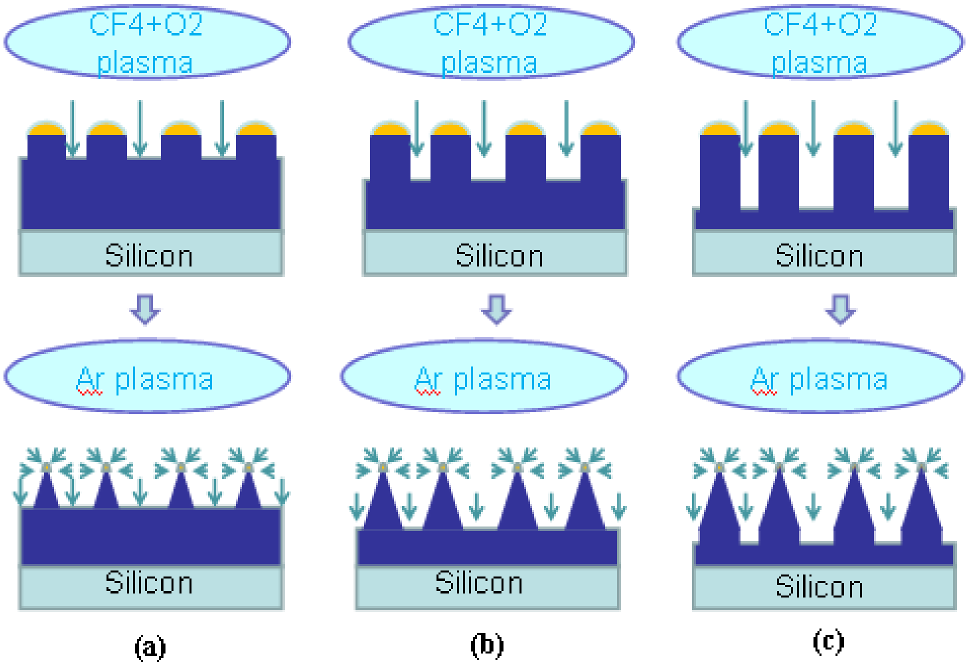

Figure 4.5: Schematic illustration of the base of the fabricated nanocones: (a) shortest etching time (b) medium etching time, and (c) longer etching time.

In the two-step etching process, first step which used the mixture of CF_4/O_2 forms the nanopillars with different heights for the different etching times as shown in Fig. 4.5. The longer etching time, the deeper the height of nanopillars. When we used the Ar gas in the second step of the etching process, Ar starts to etch the nickel nano clusters and preformed silicon nitride nanopillars isotropically. In the absence of a covering of nanoclusters, the etching rate of the top region of etched silicon would be slightly greater than that at the bottom.[49] For this reason, in the deeper nanopillar structures [i.e., Fig. 4.5(c)] the slower etching rate of the bottom region may form the longitudinal base of the nanocones.

The relations between etching time with average reflectance and structure height for nanopillars and nanocones have been shown in Figs. 4.6(a) and 4.6(b), respectively.

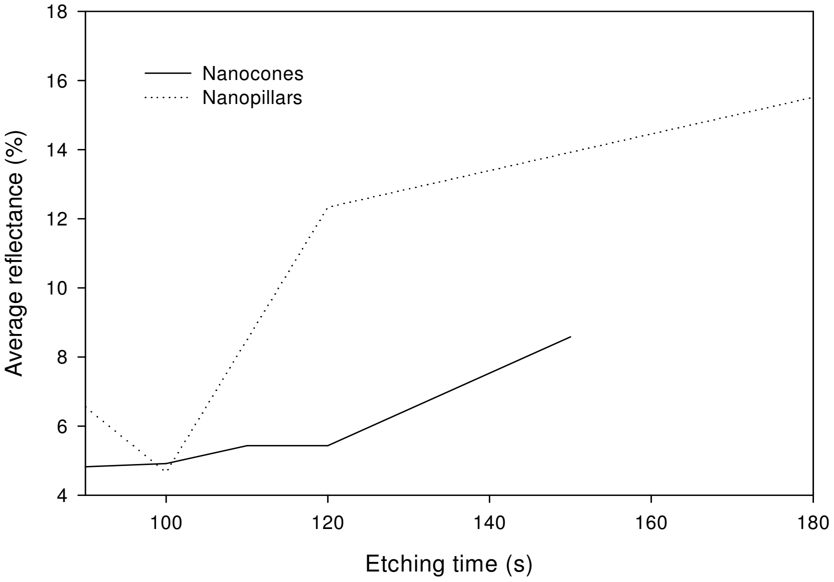

(a)

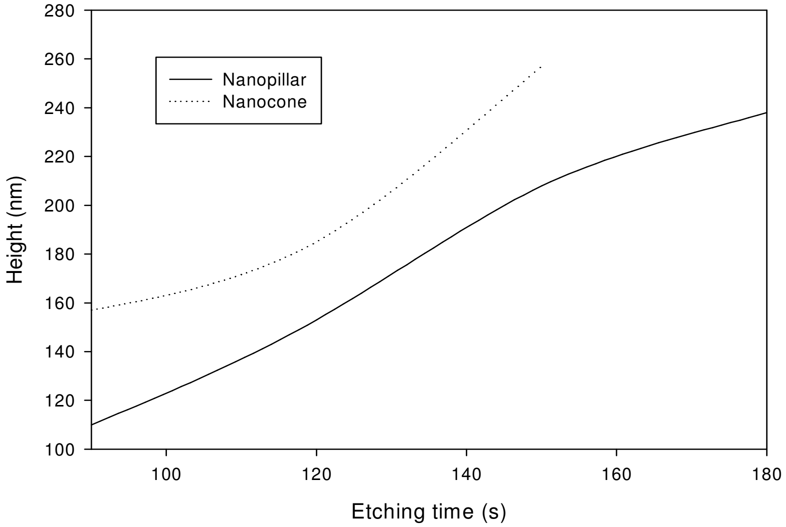

(b)

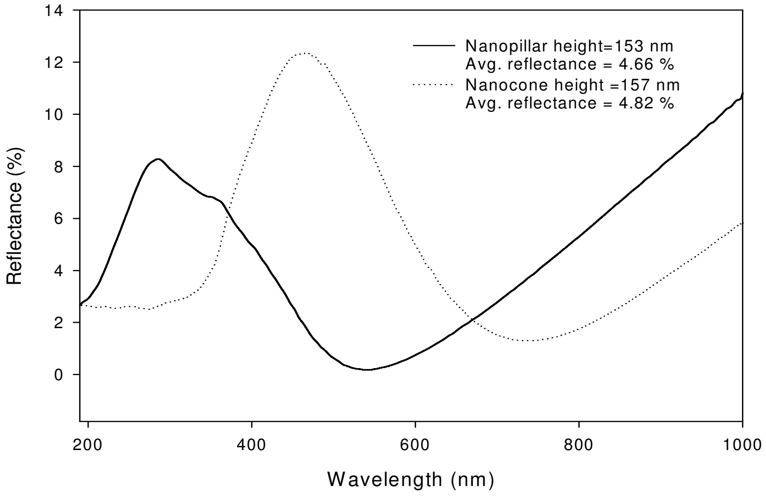

(c)

Figure 4.6 : Relations of etching time with (a) Average reflectance and (b) Structure height for the fabricated nanocone and nanopillar structures on silicon nitride film. (c) The reflectance spectra comparison of nanocone and nanopillar structures with almost same height for the wavelength from 190 to 1000 nm.

From Fig. 4.6(a), it has been observed that nanocone structures shows lesser average reflectance than the nanopillar structure when we increase the etching time. Also it has been seen from Fig. 4.6(b) that the height of the nanocone structures higher than nanopillar structures which is clearly understood effect of the second step etching process by the Ar gas. The reflectance spectra for both nanocone and nanopillar structures with almost similar height were compared in Fig. 4.6(c). It has been observed that though the average reflectance for both nanocone and nanopillar structures were less than 5 %, the average reflectance of nanopillar structures were better than the nanocone structure with similar height. Also it was observed that for the nanocone structures, the reflectance would be less than 6 % for the shorter wavelength (i.e., from 190 to 300 nm) and longer wavelength (i.e., from 700 to 1000 nm) as well. Whereas, for nanopillar structures, the reflectance would be less than 6 % for the wavelength range from 400 to 800 nm. Since both the structures could produce an average reflectance of less than 5 %, which is very good for an ARC to be applied in solar cell, it is believed that silicon nitride nano structures would be very useful for replacing the DLAR coatings and can give a better or comparable performance. But, nanocone structures have been observed to provide lower average reflectance of below 6 % for a longer range of heights as compared to nanopillar structures. So nanocone would be better structures to be used as silicon nitride sub-wavelength structures for solar cell applications due to the tolerance of wider heights variation of the structure.

4.4 Summary

An easy and scalable non-lithographic approach for creating nanocone and nanopillar structured antireflection coatings directly on silicon nitride using nickel nano cluster and ICP etching method for the solar cell application have been developed. The one step ICP etching process using a gas mixture of CF_4/O_2 can produce nanopillar structures and two step etching process using gas mixture of CF_4/O_2 in first step and Ar in second step can produce nanocone structures on silicon nitride film using nickel self assembled nickel nanocluster mask. The measured reflectance for both the structures shows a great promise to be used in solar cell to improve the efficiency because of its lower average reflectance of less than 5 %. Nanocone structures have been observed to provide lower average reflectance of below 6 % for a longer range of heights as compared to nanopillar structures. So it can be concluded that nanocones are better structures to be used as silicon nitride sub-wavelength structures for solar cell applications due to the tolerance of wider heights variation of the structure.

Chapter 5

Solar Cell Fabrication

In this chapter, we will present our preliminary result of the fabricated silicon solar cell with silicon nitride SWS and will compare with the silicon solar cell with silicon nitride SLAR. A brief description of the fabrication method will be presented which was carried out in collaboration with MOTECH Inc., Tainan.

5.1 Fabrication Process

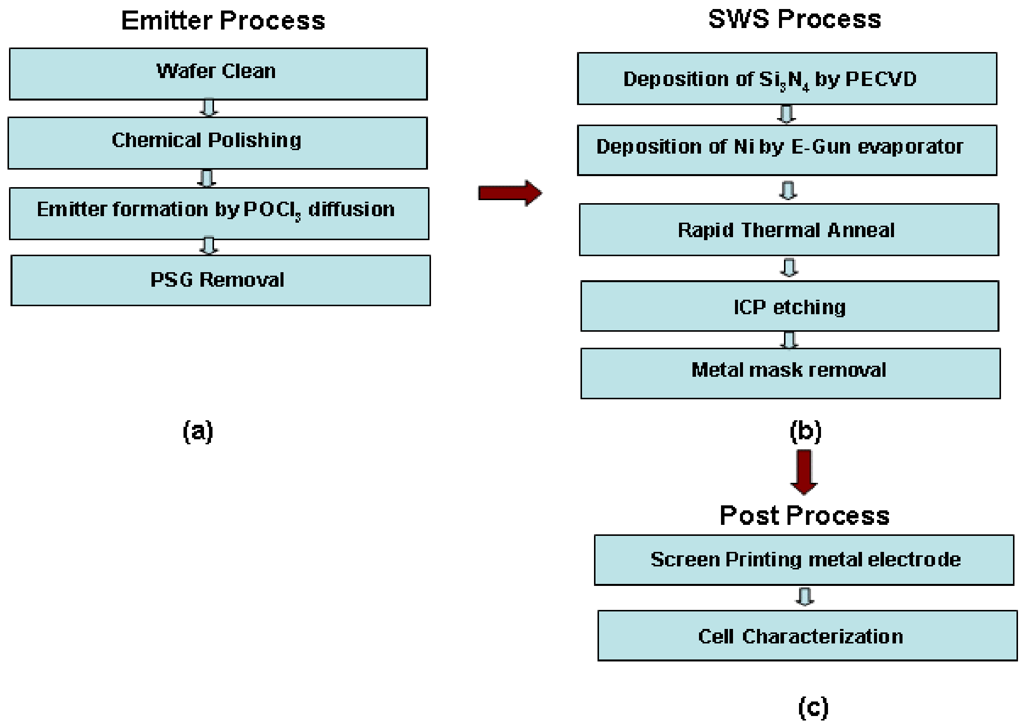

Figure 5.1: Fabrication process steps for Solar Cell with SWS (a) Emitter process (done at MOTECH Lab) (b) SWS Process (done at CSDLAB) (c) Post process (done at MOTECH Lab).

The flow chart of the fabrication process for a silicon solar cell with silicon nitride SWS is shown in Fig. 5.1. This fabrication was done by CSDLab in collaboration with MOTECH Inc., Tainan. As shown in Fig. 5.1, the part shown in Fig. 5.1(a) and (c) were done at laboratory of MOTECH Inc., Tainan and part shown in Fig. 5.1(b) was done in our compound semiconductor laboratory (CSDLab).

First, p-type silicon wafer was cleaned with H_2SO_4/H_2O_2 and followed by chemical polishing to remove surface damage. Then emitter was formed by phosphorous diffusion by supplying phosphorous trichloride oxide ($POCl_3$) to the silicon wafer. In this process, p-type silicon wafer was loaded into quartz boat which was slowly moved into the middle of a fused quartz tube in a resistance-heated horizontal furnace. Furnace temperature for the diffusion was held at about 900 °C. Nitrogen was used as a carrier gas. During the diffusion process the following reaction takes place to form phosphosilicate glass (PSG):

$$\begin{aligned} 4POCl_3 + 3O_2 &\rightarrow 2P_2O_5 + 6Cl_2 \\ 2P_2O_5 + 5Si &\rightarrow 4P + 5SiO_2 \end{aligned} \tag{41}$$

When a PSG is deposited on silicon substrate, phosphorous starts to diffuse into the bulk and emitter was formed. Then, PSG was removed by dipping the wafer in buffered 10% HF solution for about a minute. The details of the fabrication are not reported here because of some confidential issue.

Then, in our CSDLab, the silicon nitride SWSs were formed on the front surface of the solar cell using the fabrication process described in chapter 3, which was briefly described in Fig. 5.1(b).

After the SWS process was done, the post processing of the cell was done at laboratory of MOTECH Inc., Tainan again. The electrodes were formed by standard screen printing method and the cell characterization was performed to get the open circuit voltage (V_{OC}), short-circuit current density (J_{SC}), efficiency (η), and fill factor (FF) under AM1.5G conditions.

5.2 Results and Discussion


(a) (b)

Figure 5.2: Fabricated Silicon Solar Cell with (a) Si_3N_4 SLAR and (b) Si_3N_4 SWS.

The measured results tabulated in Table 4. The measured results for the fabricated silicon solar cell with silicon nitride SWS and silicon solar cell with silicon nitride single layer antireflection (SLAR) coating has been compared in Table 4. It has been observed that the V_{OC} value of the SWS solar cell is decreased by 0.001 V as compared to SLAR solar cell. Also, the fill factor of the SWS solar cell is decreased by 0.04% compared to SLAR solar cell. But, the J_{SC} and efficiency of SWS has been improved by 2.9 V and 1.09% as compared to SLAR solar cell. The decrease of FF suggests that there must be some insufficient electrical contact, which is also confirmed by the high reverse current of the SWS solar cell compared to SLAR solar cell. So there is a need to improve the fabrication process specifically the post process steps of Fig. 5.1(c).

Table 5: Measured Solar Cell parameters for Silicon Nitride SLAR and Silicon Nitride SWS. The difference is also tabulated.

	V_{OC} (V)	J_{SC} (mA/cm^2)	FF	Efficiency (%)	I_{rev} (A)
Si_3N_4 SLAR	0.596	30.8	64.24	11.77	0.22
Si_3N_4 SWS	0.595	33.7	64.2	12.86	0.63
Difference	-0.001	+2.9	-0.04	+1.09	+0.41

The increase of efficiency by 1.09% for a SWS solar cell confirms our simulated results as described in chapter 2. Since the results obtained so far is preliminary result, we expect that the efficiency can be improved more if the post process steps of the Silicon solar cell with silicon nitride SWS will be improved significantly.

5.3 Summary

A silicon solar cell with silicon nitride SWS has been fabricated. The preliminary results shows an improvement of 1.09% in cell efficiency compared to a solar cell with 80 nm silicon nitride single layer antireflection coating. This result is agreed with our simulated results discussed in chapter 2. It is believed that by improving the post processing in solar cell fabrication, the efficiency can further be improved.

Chapter 6

Conclusions and Future Works

6.1 Conclusion

In this thesis, we have presented simulation and fabrication results of designed silicon nitride sub-wavelength structures for solar cell applications.

Using the results of rigorous coupled wave analysis simulation for the pyramid, cone, parabola and cylinder shaped silicon nitride sub-wavelength structures, the ratio of silicon nitride sub-wavelength structures height and non-textured part of silicon nitride has been optimized. The reflectance results for the optimized sub-wavelength structures have been compared in terms of effective reflectivity. From the study of different shaped Si_3N_4 SWS, the cone shaped SWS shows the lowest effective reflectance for same volume as compared to pyramid, cylinder and parabola shaped Si_3N_4 SWSs.

Then lowest effective reflectivity sub-wavelength structures were compared with previously optimized 80nm Si_3N_4 SLAR and 80 nm / 100 nm Si_3N_4 / MgF_2 DLAR. A low effective reflectivity of 3.43% can be obtained for a silicon nitride SWS height and non-etched layer of 150 nm and 70 nm respectively, which is less than 80 nm Si_3N_4 SLAR of 5.41% and comparable with Si_3N_4 / MgF_2 DLAR of 5.39%.

Based on our simulation result, we found a great potential of Si_3N_4 SWS to increase the efficiency of silicon solar cell as compared to single layer Si_3N_4 ARC by reducing the reflection. So, an easy and scalable non-lithographic approach for creating nanocone and nanopillar structured antireflection coatings directly on silicon nitride using nickel nano cluster and inductively coupled plasma etching method for the solar cell application have been developed. The one step ICP etching process using a gas mixture of CF_4/O_2 can produce nanopillar structures and two step etching process using gas mixture of CF_4/O_2 in first step and Ar in second step can produce nanocone structures on silicon nitride film using nickel self assembled nickel nanocluster mask.

We observed the lowest average reflectance for the wavelength from 190 nm to 1000 nm of 4.66 % for the Si_3N_4 nanopillar using ICP with CF_4/O_2 etching gas and etching time of 120 sec for average height of 155 nm. Similarly, for the wavelength from 190 nm to 1000 nm, lowest average reflectance of 4.82 % has been achieved for the Si_3N_4 nanocone structure using ICP with CF_4/O_2 etching gas and etching time of 100 sec in first step followed by Ar etching for 90 sec in second step.

The measured reflectance for both the structures shows a great promise to be used in solar cell to improve the efficiency because of its lower average reflectance of less than 5 %. Nanocone structures have been observed to provide lower average reflectance of below 6 % for a longer range of heights as compared to nanopillar structures. So it can be concluded that nanocones are better structures to be used as silicon nitride sub-wavelength structures for solar cell applications due to the tolerance of wider heights variation of the structure, which is also seen before from our calculations.

A silicon solar cell with silicon nitride SWS has been fabricated. The preliminary results shows an improvement of 1.09% in cell efficiency compared to a solar cell with 80 nm silicon nitride single layer antireflection coating. This result is agreed with our simulated results. It is believed that by improving the post processing in solar cell fabrication, the efficiency can further be improved. Therefore, For the consideration of working wavelength region of silicon-based solar cells, the SWS with height of 140 - 160 nm is suitable as the antireflective structure and believed to increase the solar cell performance as compared to solar cell w/ SLAR structure.

6.2 Future Work

1. There is a need of study of silicon nitride sub-wavelength structures with non-periodic nature with different shape effects to get the exact calculation of reflectance.

2. More theoretical study is needed with different TE and TM wave in to consideration for more accurate results. In our calculation we have considered only TE wave.
3. Genetic algorithm or swarm optimization process can be used with PC1D calculation to accurate prediction of the electrical characteristics of solar cell.
4. Since the process developed for silicon nitride sub-wavelength structure works at high temperature (i.e. 850 ^{o}C), the process is not suitable for fabrication of silicon nitride SWS on GaAs surface. So there is need to develop a new fabrication method which can use low temperature rapid thermal annealing to form nanomasks.
5. Although, the preliminary results obtained from our silicon solar cell fabrication using silicon nitride sub-wavelength structures show a great promise in efficiency improvement compared to silicon nitride single layer antireflection coated silicon solar cell, the efficiency of silicon solar cell is lower as compared a commercial silicon solar cell available in market. This is believed to the low electrical contact formed between electrode and SWS surface. So, more work is needed in electrode formation in the process of solar cell fabrication to improve the electrical contact of the solar cell so that the efficiency of the solar cell will be improved.

Appendices

Main Entrance for SWS Reflection Calculation

```
% Initialization
inFP = fopen('AM15G.txt','r');
inputA=[];
for i=1:100000
    line=fgetl(inFP);
    if line == -1  %check if file ends or not
        break;
    end
    [last_token,ext] = strtok(line);
    inputA(i,1)=str2num(last_token);
    [last_token,ext] = strtok(ext);
    inputA(i,2)=str2num(last_token);
end
fclose(inFP);

lambda = [400:5:1000];
%lambda=190+64;

tmp_A=[];
tmp=1;
for k= 1 : size(lambda,2)
    for j=tmp : 1 : size(inputA,1)
        if lambda(1,k) == inputA(j,1)
            tmp=j;
            tmp_A(k,:)=inputA(j,:);
            break;
        end
    end
end
inputA=tmp_A;

nm = 10^(-9);                  % nanometer value
```

```
nc = 2.03;

hc = (6.63*10^34)*(3*10^8);

lamda1 = 1.1071*10^(-6);

eps = 1.16858 * 10^1;

A = 9.39816*10^(-13);

B = 8.10461*10^(-3);

theta = 0;

nc = 2.1;
theta = 0;

% Calculate the reflectance with given height and wavelength

lambda = [400:5:1000];

diameter = 50 * nm;
height_array = [10:5:250];
pyrlen = diameter;
s_array = [10:5:250];

inFP = fopen('test.txt','w');

for height = height_array
    for s = s_array
        for k = 1: size(lambda, 2)
            ns(k) =
sqrt(eps+(A/(lambda(k)*nm)^2)+((B*(lamda1^2))/(((lambda(k)*nm)^2)-lam
da1^2)));
% ref(k) = (shape, refractive index of Si3N4, refractive index of Si,
non-etched Si3N4, Base Diameter, Angle of incidence, height of SWS,
wavelength)
```

```
            ref1(k) = rcwa2(2, nc, ns(k), s*nm, diameter, theta,
(height+s)*nm, lambda(k)*nm, pyrlen);
            rlambdanlambda(k)=(ref1(k)*inputA(k,2))/(hc/lambda(k));
            nlambda(k)= inputA(k,2)/(hc/lambda(k));
        end
        sum_nlambda=sum(nlambda*5)/(1000-400);
        eff_ref1=sum(rlambdanlambda*5)/(1000-400);
        eff_ref=eff_ref1/sum_nlambda;
        savefile =
strcat('_height=',num2str(height),'_s=',num2str(s),'_ref=',num2str(ef
f_ref),'.txt');
        fprintf(inFP,'%d\t %d\t %f\n',height,s,eff_ref);

        datamat = zeros(size(lambda,2), 2);
        datamat(:, 1) =  lambda';
        datamat(:, 2) =  ref1';

        save(savefile, 'datamat', '-ASCII');

    end
end
fclose(inFP);
```

Function for Calculation of Reflectance

```
% shape: 0 = pyramid 1 = nipple cylinder 2 = parabola 3 = Cone

function ref = rcwa(shape, nc, ns, s, diameter, theta, height, lambda,
leng)

nm = 10^(-9);                       % nanometer value

nair = 1.0;                         % refractive index of air

layers = 100;                       % number of layers in the nipple

if (shape == 1)
```

```
    layers = 2;
end

layer_width = (height-s) / (layers-1);  % average layer height

d = ones(layers,1);             % height of each individual layer

n = ones(layers, 1);

r = ones(layers, 1);

% The normalized electric field(in the y-direction) for the input and
% output regions and in each of layers may be written as

% E0=[exp(-jk1z)+R*exp(jk1z)]exp(-jkz), z<=0
% El={Pl*exp[-k0*gamma1(z-D(l-1))]+Ql*exp{-j[kx*x+k2z(z-Dl)]}, z>=DL
% Et=T*exp{-j[kx*x+k2z(z-DL)]}

k0  = 2  * pi / lambda;
kx  = k0 * nair * sin(theta);
k1z = k0 * nair * cos(theta);
k2z = k0 * sqrt(ns^2 - nair^2 * sin(theta)^2);

% Determine the refractive index for each layer

outputdata=[];

for k = 1 : layers
    % Dl= summation over p=1 to l dp
    h = (1-k/(layers-1)) * (height-s);
    if (shape==0)       % pyramid fill factor
        f = 4 * inv_profile(shape, leng, height, h)^2 ...
            /(sqrt(3)*diameter^2);
     elseif (shape==1) % nipple cylinder
        f = pi * inv_profile(shape, leng, height, height-h)^2 ...
                /(sqrt(3)*diameter^2);
    elseif (shape==2) % parabola
        f = pi * inv_profile(shape, leng, height, h)^2 ...
```

```
            /(sqrt(3)*diameter^2);
    elseif (shape==3) % cone
        f = pi * inv_profile(shape, leng, height, h)^2 ...
            /(sqrt(3)*diameter^2);
    end
    n(k) = efi(nc, nair, f);
    d(k) = layer_width;
 % rk=j[nk^2-n1^2*sin(theta)^2]^(1/2)
    r(k) = i * sqrt(n(k)^2 - nair^2 * sin(theta)^2);

    outputdata(:)=n(k);
end
    n(layers)= efi(nc, nair, 1);
    d(layers)= s;
    r(layers)=i * sqrt(n(layers)^2 - nair^2 * sin(theta)^2);


d_new=d;
for ii=1:length(d)
   d_new(ii)=sum(d(1:ii));
end

fid=fopen('n.txt','w');
fprintf(fid,'%d\t %d \n',[n d_new]');
fclose(fid);



vec0 = [1; i * k1z/k0];
vecr = [1; -i * k1z/k0];
vect = [1; i * k2z/k0];
matt1 = zeros(2,2);
matt2 = zeros(2,2);




% loop over all layers from bottom to top
for k = layers : -1 : 1
```

```
   % Constrcut the k-th layer matrices

   matt1(1,1) = 1;
   matt1(1,2) = exp(-k0*r(k)*d(k));
   matt1(2,1) = r(k);
   matt1(2,2) = -r(k)*exp(-k0*r(k)*d(k));

   matt2(1,1) = exp(-k0*r(k)*d(k));
   matt2(1,2) = 1;
   matt2(2,1) = r(k)*exp(-k0*r(k)*d(k));
   matt2(2,2) = -r(k);

   % Multiply the vector vect with the matrix for the new vector
   vect = matt1 * inv(matt2) * vect;

end

matrixa = [-vecr vect];

vecsol = inv(matrixa) * vec0;

ref = vecsol(1) * conj(vecsol(1));

return

% This is the inverse of the profile function

function r = inv_profile(shape, diameter, height, z)

if (shape == 0)         % pyramid
     r = (diameter/2)*(1-(z/(height)));
elseif (shape == 1)   % cylinder
     r = diameter/2;
elseif (shape == 2) % paraboloid
     r = (diameter/2)*sqrt(1-z/(height));
elseif (shape == 3) % cone
     r = (diameter/2)*(1-z/(height));
end
```

```
return

%----------------------------------------------------------------
% Calculate the effective refractive index of the given layer

function ne = efi(nc, nair, f)

g = (1-f+f*(nc^2))*(f+(1-f)*nc^2)+nc^2;
l = 2*(f+(1-f)*nc^2);
ne = sqrt(abs(g/l));

return
```

References

[1] Jeffrey A. Mazer: *Solar Cells: An Introduction to Crystalline Photovoltaic Technology* (Kluwer Academic Publishers, USA, 1997).

[2] E.Fred Schubert: *Light-Emitting Diodes* (Cambridge University Press) 409-412.

[3] F.W. Sexton, Solar Energy Mater. Sol. Cells **7** (1991) pp. 1.

[4] R. Kishore, S.N. Siingh, B.K. Das, Sol. Energy Mater. Sol. Cells **26** (1992) pp. 27.

[5] Z. Chen, P. Sana, J. Salami, A. Rohatgi, IEEE Trans. Electron Devices **40** (1993) pp. 1161.

[6] K. Ram, S.N. Singh, B.K. Das, Renewable Energy **12** (1997) pp. 131.

[7] C. Battaglin, F. Caccavale, A. Menelle, M. Montecchi, E. Nichelatti, F. Nicoletti, Thin Solid Films **351**(1999) pp. 176.

[8] U. Gangopadhyay, K. Kim, D. Mangalaraj, J. Yi, Appl. Surf. Sci. **230** (2004) pp. 364.

[9] Xi, J. Q., M. F. Schubert, et al., Nature Photonics 1 (3) (2007) pp. 176.

[10] H.A. Macleod: *Thin-Film Optical Filters* (second ed., McGraw-Hill, New York, 1990).

[11] D. Chen, Sol. Energy Mater. Sol. Cells **68** (2001) pp. 313.

[12] T. Mizuta, T. Ikuta, T. Minemoto, H. Takakura, Y. Hamakawa, T. Numai, Sol. Energy Mater. Sol. Cells **90** (2006) pp. 46.

[13] B. Paivanranta, N. Hekkila, and M. Kuittnen, J. Opt. Soc. Am. A 24, **6** (2007) pp. 1680.

[14] P. Lalanne and G. M. Morris, Nanotechnology **8 (**1997) pp. 53.

[15] Y. C. Chang, G. H. Mei, T. W. Chang, T. J. Wang, D. Z. Lin and C K Lee, Nanotechnology **18 (**2007) pp. 285.

[16] M. J. Minot, J. Opt. Soc. Am. **66** (1976) pp. 515.

[17] T. Glaser, A. Ihring, W. Morgenroth, N. Seifert, S. Schro¨ter and V. Baier, Microsystem Technologies **11** (2005) pp. 86.

[18] K. Hadobas, S. Kirsch, A. Karl, M. Acet, and E. F. Wassermann, Nanotechnology, **11** (2000) pp. 161.

[19] Y. Kanamori, M. Sasaki, and K. Hane, Opt. Lett., **24** (1999) pp. 1422.

[20] Z. N. Yu, H. Gao, W. Wu, H. X. Ge, and S. Y. Chou, J. Vac. Sci. Technol. B, **21** (2003) pp. 2874.

[21] H. Sai, H. Fujii, K. Arafune, Y. Ohshita, M. Yamaguchi, Y. Kanamori, and H. Yugami, Appl. Phys. Lett., **88** (2006) pp. 20116.

[22] Y. Inomata, Sol. Energy Mater. Solar Cells, **48** (1997) pp. 237.

[23] H. F. W. Dekkers, Opto-Elctron. Rev., **8** (2000) pp. 311.

[24] L. Lalanne and M. Hutley: *Artificial media optical properties subwavelength scale Encyclopedia of optical Engineering* (Dekker, New York, 2003).

[25] P. Yeh: *Optical Waves in Layered Media* (Wiley, New York, 1991).

[26] D. A. G. Bruggeman, Ann. Phys. **24** (1935) pp. 636.

[27] J. Zhao, M.A. Green, IEEE Trans. Electron Dev. **38** (1991) pp. 1925.

[28] H. A. Macleod: *Thin-Film Optical Filters* (3rd ed., Institute of Physics, Bistol, 2001).

[29] L. M. Brekhovshikh: *Waves in Layered Media* (Academic, New York, 1960).

[30] K. L. Chopra and S. R. Das: *Thin film solar cells* (Plenum Press, New York and London 1983).

[31] C.-H. Sun, W.-L. Min, N. C. Linn, and P. Jiang, Appl. Phys. Lett. **91** (2007) pp. 231105.

[32] S. Khedim, A. Chiali, B. Benyoucef, and N. E. Chabane Sari, in: Proc. Revue des Energies Renouvelables ICRESD-07 Tlemcen (2007) pp. 337.

[33] D. N. Wright, E. S. Marstein and A. Holt, in: Proc. The 31st IEEE Photovoltiac Specialists Conf., Orlando Fl (2005) pp. 1237.

[34] http://rredc.nrel.gov/solar/spectra/am1.5/ASTMG173.html

[35] D. G. Stavenga, S. Foletti, G. Palasantzas, and K. Arikawa, Proc. R. Soc. London, Ser. B **273**, (2006) pp. 661.

[36] C. G. Bernhard, W. H. Miller and A. R. Møller, Acta Physiol. Scand. **63** (Suppl.243), (1965) pp. 1.

[37] P. A. Basore: *PC-1D Installation Manual and User's GuideVersion 3.1* (Sandia Report, Sandia National Laboratories, California, 1991)

[38] D. A. Clugston and P. A. Basore, in: Proc. The 26th IEEE Photovoltiac Specialists Conf., Anaheim (1997) pp. 207.

[39] P.A. Basore, IEEE Trans. on Electron Devices **37**, (1990) pp. 337.

[40] http://www.semiconductor.net/article/CA6572786.html

[41] S. Aggarwal, S. B. Ogale, C. S. Ganpule, S. R. Shinde, V. A. Novikov, A. P. Monga, M. R. Burr, R. Ramesh, V. Ballarotto and E. D. Williams, Appl. Phys. Lett. **78** (2001) pp. 1442.

[42] C. Bower, O. Zhou, W. Zhu, D. J. Werder and S. Jin, Appl. Phys. Lett. **77** (2000) pp. 2767.

[43] J. D. Carey, L. L. Ong, S. R. P. Silva, Nanotechnology **14** (2003) pp. 1223.

[44] B. G. Prevo, E. W. Hon, and O. D. Velev, J. Mater. Chem. **17**, (2007) pp. 791.

[45] P. Lalanne and G. M. Morris, Nanotechnology **8**, (1997) pp. 53.

[46] C. Aydin, A. Zaslavsky, G. J. Sonek, and J. Goldstein, Appl. Phys. Lett. **80**, (2002) pp. 2242.

[47] Y. Kanamori, E. Roy, and Y. Chen, Microelectron. Eng. **78-79**, (2005) pp. 287.

[48] Y. Kanamori, M. Sasaki, and K. Hane, Opt. Lett. **24**, (1999) pp. 1422.

[49] H. Xiao: *Introduction to Semiconductor Manufacturing Technology* (Prentice Hall, Upper Saddle River, NJ, 2001).

[50] A. Luque and S. Hegedus: *Handbook of Photovoltaic Science and Engineering* (John Wiley & Sons, Ltd, ISBN: 0-471-49196-9, 2003).

[51] L. L. Kazmerski, Journal of Electron Spectroscopy and Related Phenomena **150** (2006) 105.

Curriculum Vita

Kartika Chandra Sahoo

Nationality: Indian
e-mail: kartiknctu@gmail.com
phone #: +886 972145824

Dept. of Materials Science & Engineering
National Chiao-Tung University
1001 Ta-Hsueh Rd
Hsinchu, Taiwan, R.O.C. 3001

RESEARCH INTERESTS

Advanced semiconductor devices, Nanotechnology, Quantum dots and Nano structures to Solar cells, Hetero-structure Device Modelling, Semiconductor device simulation: model and programming, TCAD simulation of CMOS devices.

EDUCATION

MSc. in Electronics Science (2 years degree) August 1998-July 2000
Department of Electronics Science
Berhampur University, Berhampur, Orissa, India

BSc. in Physics (3 years degree) August 1995-July 1998
Government Science College, Chatrapur
Berhampur University, Berhampur, Orissa, India

WORK EXPERIENCES

1. Graduate Research Assistant, Materials Science & Engineering Department, ***National Chiao-Tung University*** Taiwan
   Advisor: Prof. Edward Yi Chang
   Project Sponsor: Motech Inc., Taiwan
   Project Title: ***Novel double layer and sub-wavelength anti-reflective coatings for high efficiency crystalline silicon solar cells.***
   July 2008 to April 2009

2. Graduate Research Assistant, Materials Science & Engineering Department, ***National Chiao-Tung University*** Taiwan
   Advisor: Prof. Edward Yi Chang
   Project Sponsor: ITRI, Taiwan

Project Title: ***The study of silicon nitride antireflective coating for high efficiency solar cell application.***

July 2005 to Feb 2006

3. Project Assistant, ***National Institute of Science & Technology,*** Berhampur, Orissa, India.

   PI: Prof. Ajit Kumar Panda

   Project Sponsor: University Grant Comission, India

   Project Title: ***Study of effect of interface properties on high frequency behavior of GaN based MODFET to use in VLSI circuits.***

   Oct 2002 to Aug 2004

SEMICONDUCTOR PROCESS AND TOOL EXPERIENCE

Semiconductor materials: GaAs, (In, Al)GaAs, Silicon Nitride, Si

Working in compound semiconductor devices lab (Class 1000) of Department of materials science & engineering, *NCTU, Taiwan*. I am having expertise on the following systems: -

- E-Gun Evaporation system
- Thorough knowledge of operation and maintenance of clean work benches (class 100) and clean rooms (class 1000).
- ABM lithography System.
- HEMT process.
- Four Probe DC measurements System.
- X-ray Diffraction analysis tool
- Atomic Force Microscope (AFM) tool.
- Making the TEM sample.
- Metal Organic Chemical Vapor Deposition (MOCVD) System (Home made System)
- Plasma Enhanced Chemical Vapor Deposition (PECVD) System (STS 300PC series-310PC)

COMPLEMENTARY INFORMATION

LANGUAGES:	**English** (R-W-S)
	Oriya (native) (R-W-S)
	Hindi (R-W-S)
	Chinese, (S Beginners Level)

SOFTWARE PACKAGES: Experience in SILVACO TCAD, ISE TCAD, COMSOL,
Spice, MATLAB, FORTRAN etc.

PATENT

1. "Silicon nitride sub-wavelength structure fabrication technique for high efficiency solar cell applications". Inventors: E. Y. Chang, **K. C. Sahoo**, M. K. Lin, Y. Y. Liao, and S. P. Wang,. Patent Pending (2009).

PAPERS IN INTERNATIONAL JOURNALS

1. Fabrication and Configuration Development of Sub-Wavelength Structure of Silicon Nitride for Solar Cell Application, **Kartika Chandra Sahoo**, Men-Ku Lin, Edward Yi Chang, Yiming Li, and Jin-Hua Huang, **Journal of Nanoscience and Nanotechnology**, Accepted (2009). (**IF: 1.929**)

2. Silicon Nitride Nanopillars and Nanocones formed by Nickel Nano-clusters and Inductively Coupled Plasma Etching for Solar Cell Application, **Kartika Chandra Sahoo**, Men-Ku Lin, Edward Yi Chang, Tran Binh Tinh, Yiming Li, and Jin-Hua Huang, **Japanese Journal of Applied Physics,** In Press (2009). (**IF: 1.309**)

3. Numerical Calculation of the Reflectance of Sub-wavelength Structures on Silicon Nitride for Solar Cell Application, **Kartika Chandra Sahoo**, Yiming Li, and Edward Yi Chang, **Computational Physics Communication,** 180, 1721–1729, 2009. (**IF: 2.120**)

4. Fabrication of antireflective sub-wavelength structures on silicon nitride using nano cluster mask for solar cell application, **Kartika Chandra Sahoo**, Men-Ku Lin, Edward Yi Chang, Yi-Yao Lu, Chun-Chi Chen, Jin-Hua Huang, and Chun-Wei Chang, **Nanoscale Research Letter,** 4, 680-683, 2009 (**IF: 1.731**)

5. Novel Cu/Cr/Ge/Pd Ohmic Contacts on Highly-Doped n-GaAs, **Kartika Chandra Sahoo**, Chun-Wei Chang, Tung-Ling Hsieh and Edward Yi Chang, **Journal of Electronics Materials,** Vol. 37, No. 6, June, 2008. (**IF: 1.320**)

6. InAs/InGaAs Metamprphic High Electron Mobility Tansistor with Cu/Pt/Ti Gate and Cu airbridge, Chun-Wei Chang, Po-Chou Chen, Huang-Ming Lee, Szu-Hung Chen,

Kartik Chandra Sahoo, Edward Yi Chang, Muh-Wang Liang, Tsung-Eong Hsieh, **Japanese Journal of Applied Physics**, Vol. 46, No. 5A, May, 2007. (**IF: 1.222**)

CONFERENCE CONTRIBUTIONS

1. Finite Element Analysis of Antireflective Silicon Nitride Sub-Wavelength Structures for Solar Cell Application, Accepted in International Thin Films Conference, TACT 2009, December 14-16, 2009, Taipei, Taiwan, H. M. Lee, **Kartika Chandra Sahoo**, Edward Yi Chang, J. C. Wu, and Yiming Li

2. Design and Fabrication of sub-wavelength structure on Silicon Nitride for Solar Cell Application, Accepted to publish in Proceedings of 9th International Conference on Nanotechnology, IEEE Nano 2009, Geneoa — Italy, **Kartika Chandra Sahoo**, Yiming Li, Men-Ku Lin, Edward Yi Chang, and Jin-Hua Huang

3. Reflectance of Sub-Wavelength Structure on Silicon Nitride for Solar Cell Application, Accepted to publish in Proceedings of International conference on the SISPAD-2009, San Diego — California, **Kartika Chandra Sahoo**, Men-Ku Lin, Edward Yi Chang, Yiming Li, and Jin-Hua Huang

4. Study of Reflectance Properties of Sub-wavelength Structures on Silicon nitride for Solar cell application, Accepted to publish in Proceedings of 34th PVSC -2009, Philadelphia, PA, USA, **Kartika Chandra Sahoo**, Men-Ku Lin, Edward Yi Chang, and Jin-Hua Huang.

5. Velocity Overshoot 2D-effect in GaN based submicron Devices, Presented in CODIS-2004, JU, Kolkata, **K. C. Sahoo**, A. K. Panda.

6. SiC-based IMPATTs at Microwave and MM-wave frequency, Presented in INCURSI-2004, **K. C. Sahoo**, Suchismita Nayak, and A. K. Panda.

7. Wide band gap 6H-SiC IMPATTs to use at high frequency, Presented in APMC-2004, New Delhi, Dec 15-18, 2004, **K. C. Sahoo** and A. K. Panda.

8. Velcoity Overshoot 2D effect in submicron devices, Physics of Semiconductor Devices IWPSD –2003, Narosa Publishing House, pp. 797-799, **K. C. Sahoo**, and A. K. Panda.

9. Dynamic characteristics of SiC-based IMPATTs, Physics of Semiconductor Devices IWPSD –2003, Narosa Publishing House, pp. 794-796, **K. C. Sahoo**, D. Khadanga, and A. K. Panda.

10. Potentiality of SiC to use as IMPATTs, National Symposium on Advances in Microwaves and Light Waves (Allied Publishers), pp. 112-115, 2003, Suchismita Nayak, **K. C. Sahoo**, and A. K. Panda.

Courses Studied in Master and PhD:

- Electronic materials
- Networks & control
- Computer application to numerical methods and circuit-simulation
- Telematics
- Advanced electronic instrumentation
- Microwave theory and techniques
- Solid state devices
- Digital electronics
- Analog circuits
- Electronic instrumentation
- Microprocessor
- Signals and systems
- Communication science
- Optoelectronics
- Compound semiconductor device processing
- Surface ananlysis
- Introduction to flat panel display

Personal Profile

Date of birth : 21 July 1978

Father’s Name : Sankar Sahoo

Marital Status : Married

Sex : Male

Permanent Address : At/ Po- Govindpur, Dhenkanal,
Orissa, India, 759027

Declaration

I declare that the above statements made by me are true to best of my knowledge and belief.

Signature:___Kartika Chandra Sahoo____

Certificate of Achievement

The National Chiao Tung University (NCTU) hereby certifies ***Kartika Chandra Sahoo*** has served as ***Vice President of NCTU Foreign Student Association*** from June 1, 2007 to April 30, 2008. His effort has been proved to successfully assist in completing all responsibility and commitment involved with serving the international student community at National Chiao Tung University.

Signed on the day of June 20, 2008

Chung-Yu Wu

Chung-Yu Wu, President
National Chiao Tung University

證　書

(97)交大國服字第 014 號

茲證明 **哥帝克**同學擔任國立交通大學九十六學年度 **外籍生學會副會長** 之職務，任期為民國九十六年六月一日至民國九十七年四月三十日止。其任內認真負責，表現優異，特發此證以資證明。

國立交通大學校長 吳重雨

中華民國 九十七 年 六 月 二十日